Journal of Medicinal Chemistry

pubs.acs.org/jmc

Article

Inclusion of Nitrofurantoin into the Realm of Cancer Chemotherapy via Biology-Oriented Synthesis and Drug Repurposing

Perihan A. Elzahhar,[▽] Hisham A. Nematalla,[▽] Houssam Al-Koussa, Carla Abrahamian, Amira F. El-Yazbi, Larry Bodgi, Jolie Bou-Gharios, Joyce Azzi, Joelle Al Choboq, Hala F. Labib, Wassim Abou Kheir, Marwa M. Abu-Serie, Mohamed A. Elrewiny, Ahmed F. El-Yazbi,* and Ahmed S. F. Belal*

Cite This: *J. Med. Chem.* 2023, 66, 4565−4587

Read Online

ACCESS | Metrics & More | Article Recommendations | Supporting Information

ABSTRACT: Structural modifications of the antibacterial drug nitrofurantoin were envisioned, employing drug repurposing and biology-oriented drug synthesis, to serve as possible anticancer agents. Eleven compounds showed superior safety in non-cancerous human cells. Their antitumor efficacy was assessed on colorectal, breast, cervical, and liver cancer cells. Three compounds induced oxidative DNA damage in cancer cells with subsequent cellular apoptosis. They also upregulated the expression of Bax while downregulated that of Bcl-2 along with activating caspase 3/7. The DNA damage induced by these compounds, demonstrated by pATM nuclear shuttling, was comparable in both MCF7 and MDA-MB-231 (p53 mutant) cell lines. Mechanistic studies confirmed the dependence of these compounds on p53-mediated pathways as they suppressed the p53−MDM2 interaction. Indeed, exposure of radiosensitive prostatic cancer cells to low non-cytotoxic concentrations of compound **1** enhanced the cytotoxic response to radiation indicating a possible synergistic effect. *In vivo* antitumor activity was verified in an MCF7-xenograft animal model.

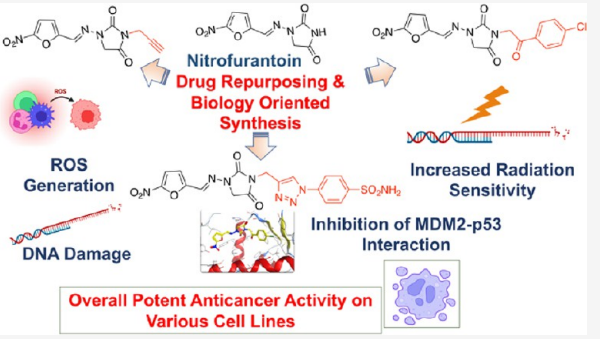

1. INTRODUCTION

Drug repurposing is a drug discovery strategy aiming at extending the application of an existing drug to treat/manage a new disorder.[1] Under the same definition lies drug design programs that use a drug as a starting material for identifying new biological targets.[1−3] A major privilege of the latter approach is the exploitation of an already well-established drug space in terms of optimized physicochemical and pharmacokinetic properties.[4] Hence, such an approach proved to be faster and more cost-effective and is associated with lower attrition rates than the traditional drug development process.[5]

In particular, in the area of cancer research, drug repurposing manifested itself as a fertile soil for the development of efficacious anticancer agents. For example, anthracyclines and thalidomide[6] are repurposed drugs that are already used in clinical practice to treat cancer. Cimetidine,[7] pravastatin,[8] clarithromycin,[9] and many COX inhibitors such as aspirin[6] are examples of repurposed drugs that proved to have anticancer activity in at least one clinical trial. Moreover, our laboratory has succeeded in repurposing the obsolete anti-amoebic iodoquinol into effective anticancer leads that modulated redox homeostasis.[2]

Over and above, we envisioned to merge the drug repurposing approach with the concept of "biology-oriented drug synthesis" (BIODS), which has received recognition from the scientific community.[10,11] The latter focuses exclusively on exploring the biological potential of already existing drug candidates after structural alterations through the application of a straightforward synthesis procedure involving only one or two steps.[10,12]

Indeed, cancer is a multidimensional disorder with redundant compensatory pathways and multiple resistance mechanisms. Hence, it remains highly incurable despite the untiring efforts exerted by different drug research groups around the globe. According to Globocan 2020,[13] the number of reported new cases was 19,292,789 while around 9,958,133 deaths occurred due to cancer of all types.

Of particular interest to this study, nitrofurantoin is a pharmacophore-rich molecule that has pro-oxidant properties and is engaged in the mitochondrial reactive oxygen species (ROS) pathway, resulting in oxidative stress, which accounts for its anticancer activity.[3,14] Intriguingly, chemical derivatization of nitrofurantoin gave rise to beneficial anticancer lead compounds, acting by induction of apoptosis.[14]

Received: August 25, 2022
Published: March 15, 2023

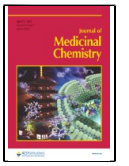

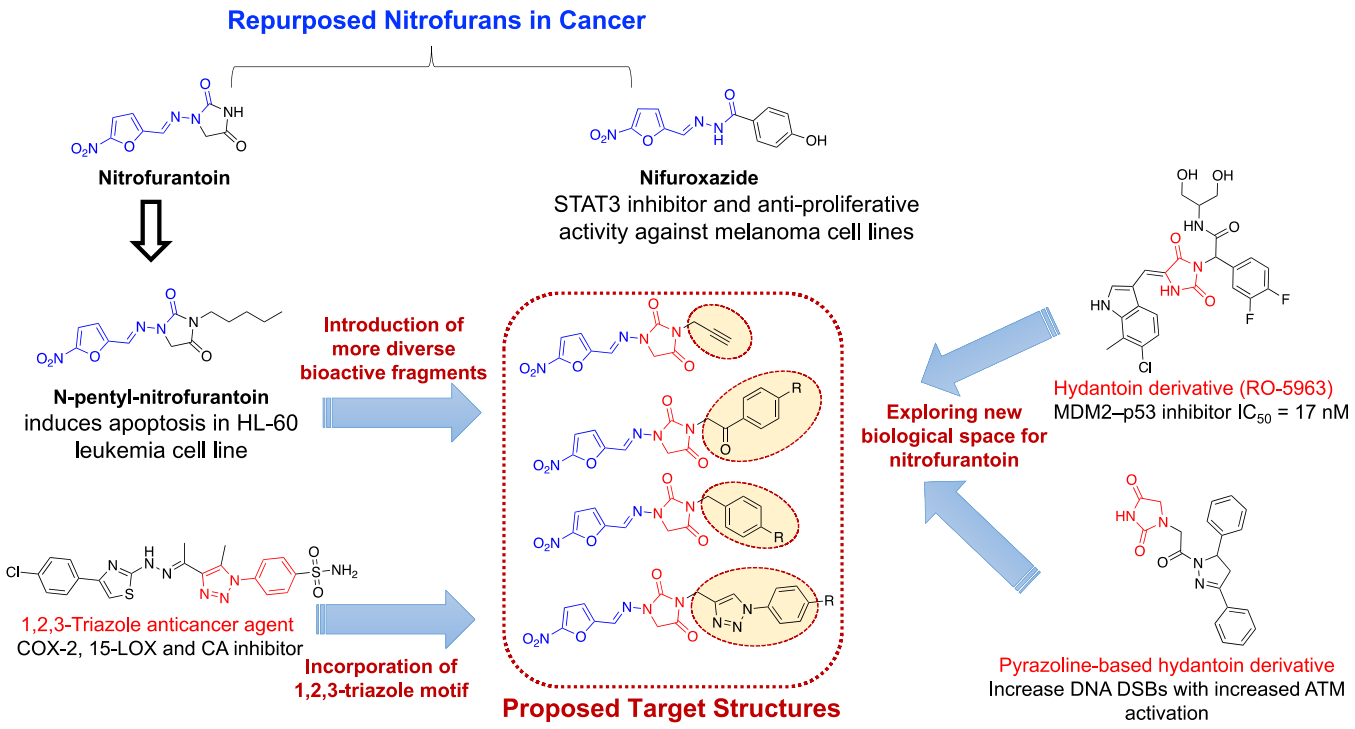

Figure 1. Rationale for the design of new nitrofurantoin derivatives.

Within the context of apoptosis in cancer cells, p53, also known as "the guardian of the human genome", controls the expression of downstream genes that are known to be implicated in tumor formation, and hence it is not surprising that over 50% of human malignancies possess p53 mutations.[15] Furthermore, p53 function is commonly disrupted in cancers with wild-type p53 alleles either due to mutations in related positive controllers or upregulation of negative ones.[16] Mammalian cells that have DNA double-strand breaks, such as those caused by erroneous growth signals or ionizing radiation, are under the control of the p53 tumor suppressor.[16] Both the type of the cell and its level of damage determine whether the activated p53 protein initiates apoptosis or arrests cell growth.[16] Consequently, the inability of a damaged cell to engage in growth arrest or apoptosis, or to respond to DNA damage by other p53-mediated pathways, might result in abnormal cell development and carcinogenesis.[16]

Importantly, expression of proteins involved in cell cycle control, DNA repair, angiogenesis prevention, antioxidant activity, metabolic regulation, and apoptosis inducers are all triggered by p53.[15] Moreover, p53 controls the mitochondrial apoptosis mechanism, which is the primary route of cell death for most cells.[17] A decrease in the thickness of the mitochondrial membrane is caused by proapoptotic proteins such as Bax as well as p53 itself.[18] As a result, mitochondrial cytochrome C is liberated into the cytoplasm initiating a cascade of caspase activation due to interaction of the former with cytoplasmic proteins.[18] Cell death ultimately occurs since caspases damage the cytoskeleton.[15]

When the cellular stress response develops, p53 levels upsurge, resulting in apoptosis or cell cycle arrest.[15] The MDM2 protein, the negative master regulator of the p53 protein, adjusts p53 levels in the absence of physiological stress. MDM2 binds to p53, facilitating its ubiquitination and subsequent degradation.[19] Therefore, targeting MDM2/p53 interaction emerged as an interesting strategy for cancer therapy.

From a different perspective, ATM (or ataxia telangiectasia mutated protein) is one of the key kinases engaged in the cellular response to DNA double-strand breaks (DSBs) that ensue, due to ionizing radiation.[20] Following the induction of DNA DSBs, ATM phosphorylates p53 on Ser15.[21] As well, an essential ATM downstream target, checkpoint kinase 2 (CHK2), phosphorylates p53 on Ser20. Phosphorylated p53 prevents Mdm2-mediated ubiquitination and degradation.[22] In addition, ATM directly phosphorylates Mdm2, which contributes to p53 accumulation and stabilization.[20] In doing so, it triggers the expression of genes implicated in cell cycle checkpoint activation as well as apoptosis.[20,23]

Guided by the aforementioned framework, several members of the nitrofuran family of drugs that have been employed in the realm of cancer chemotherapy were adopted as lead compounds.[24] First of which, nifuroxazide demonstrated STAT3 inhibitory and antiproliferative activities against melanoma cell lines.[25] Along the same track and as a typical illustration for the application of derivatized repurposed drugs in oncology, *N*-pentyl nitrofurantoin was found to induce apoptosis in the HL-60 leukemia cell line via upregulating Bax and downregulating Bcl-xL expression[14] (Figure 1).

Over and above, the hydantoin derivative (RO-5963) is a potent MDM2−p53 inhibitor (IC_{50} = 17 nM)[26]). Moreover, a pyrazoline-based hydantoin analog exhibited significant antitumor activity in the HT-29 animal xenograft model. It also induced DNA damage in K562 cells and produced a significant increase of DNA double-strand breaks, which was associated with increased phosphorylation of ATM.[27] Inspired by some multi-target anticancer 1,2,3-triazole derivatives reported by our group,[28] the design of some 1,2,3-triazole nitrofurantoin derivatives was planned (Figure 1).

The latter design incorporated more diverse bioactive fragments (such as propargyl group, substituted benzyl, and phenacyl groups in addition to 4-substituted phenyl-1,2,3-triazole) at N3 of the hydantoin motif. Since drug repurposing is

https://doi.org/10.1021/acs.jmedchem.2c01408
J. Med. Chem. 2023, 66, 4565−4587

Scheme 1. Synthesis of the Target Nitrofurantoin Derivatives[a]

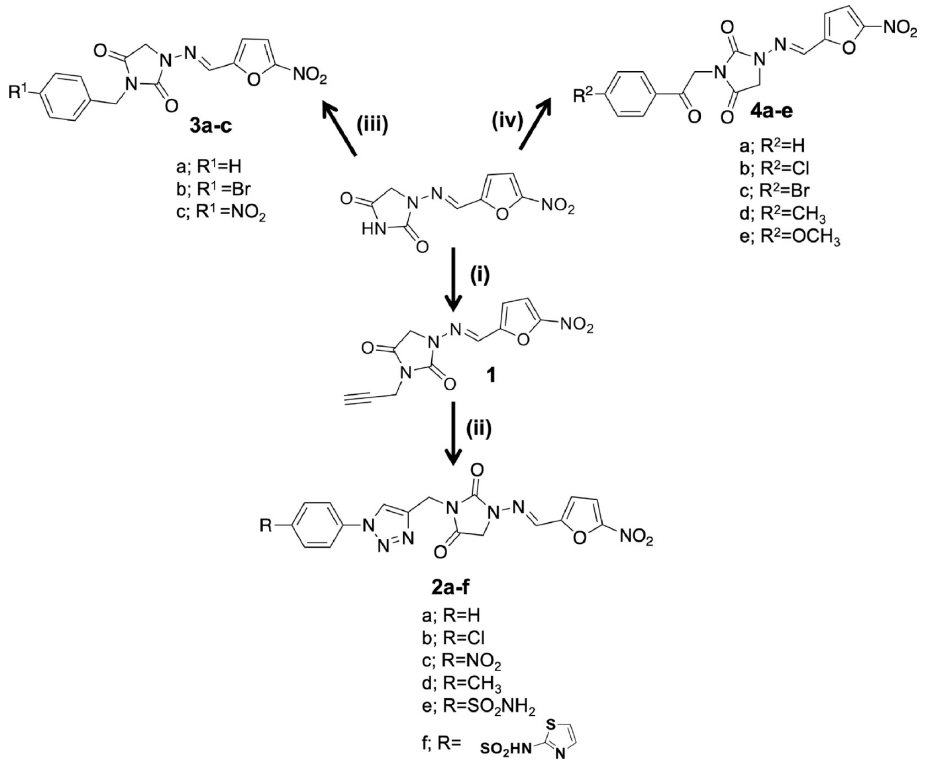

[a]Reagents and conditions: (i) $HC{\equiv}CCH_2Br/K_2CO_3$/DMF/RT, stirring overnight; (ii) 4-$R^2C_6H_4N_3$/CuAAC/DMF/RT, stirring overnight; (iii) 4-$RC_6H_4CH_2Br/K_2CO_3$/DMF/RT, stirring overnight; (iv) 4-$R^1C_6H_4COCH_2Br/K_2CO_3$/DMF/RT, stirring overnight.

a straightforward application of polypharmacology,[5] our design was attempted to achieve a multitargeting profile with the aim of expanding the biological space for the nitrofuran class of drugs. Capitalizing on the nitrofuran scaffold, we herein present a new series of nitrofurantoin antitumor derivatives that are not only apoptogenic but also inhibit MDM2/p53 interaction, enhance ATM activation, and induce DNA damage.

2. RESULTS AND DISCUSSION

2.1. Chemistry. The synthetic pathways, adopted for the preparation of final compounds, are illustrated in Scheme 1. The target compounds **1**, **3a−c**, and **4a−e** were synthesized in good yields via alkylation of nitrofurantoin with propargyl bromide, the appropriate benzyl halides, and phenacyl bromides, respectively, in the presence of anhydrous potassium carbonate in DMF. The ^{1}H NMR of **1** showed the propargylic protons' signals at δ 3.18 and 4.29 ppm, corresponding to terminal CH and CH_2, respectively. Its ^{13}C NMR demonstrated propargylic characteristic peaks at δ 28.2, 74.7, and 78.1 ppm that correspond to CH_2, CH, and quaternary carbon. Other characteristic peaks of parent nitrofurantoin appeared at their expected chemical shifts. In addition, the IR spectrum revealed the characteristic sharp band for the acetylenic−CH stretching at 3245 cm^{-1} and C≡C stretching at 2200 cm^{-1}. For the benzyl derivatives **3a−c**, their ^{1}H NMR and ^{13}C NMR spectra showed the appearance of benzylic CH_2 signals at around δ 4.6−4.8 and 42 ppm, respectively. Moreover, other proton and carbon signals characteristic for the molecule were shown at their expected chemical shifts. With respect to the phenacyl derivatives **4a−e**, the phenacyl CH_2 signals were displayed in ^{1}H NMR and ^{13}C NMR spectra at around δ 5−5.2 and 49 ppm, respectively.

Click modification of the propargyl **1** with the proper aromatic azides, using a catalytic amount of copper sulfate and sodium ascorbate in a DMF-H_2O mixture, yielded the target 1,4-disubstituted 1,2,3-triazoles (**2a−f**). Their ^{1}H NMR showed the C_5-triazole proton as a singlet at around 8.7−9 ppm, together with the disappearance of alkyne terminal CH present in the precursor.

2.2. Biological Evaluation. *2.2.1. In Vitro Cytotoxicity in the Normal Human Lung Fibroblast Wi-38 Cell Line.* All 15 newly synthesized nitrofurantoin derivatives were tested for their cytotoxicity in the normal human lung fibroblast Wi-38 cell line, using the MTT assay, to assess their safety profile in comparison to the reference drugs 5-FU and nitrofurantoin (NF).

Results recorded in Table 1 (in terms of IC_{50} and EC_{100} in μM) revealed that nine compounds (**1**, **2a**, **2d−f**, **3a**, and **4a−c**) showed higher IC_{50} values (0.216−0.306 μM) than 5-FU and NF (0.192 and 0.162 μM, respectively). With regard to EC_{100} values, 11 compounds (**1**, **2a**, **2b**, **2d−f**, **3a**, **3b**, and **4b−d**) were superior or equal to 5-FU and NF (0.027−0.11, 0.017, and 0.027 μM, respectively). It is noteworthy to mention that high IC_{50} and EC_{100} values are good safety indicators toward normal cells. Hence, compound **1** showed the highest safety margin, in terms of both IC_{50} and EC_{100} values, followed by compounds **2e** and **4b**.

2.2.2. In Vitro Anticancer Activity in Cancer Cell Lines. The *in vitro* inhibitory activities of all synthesized compounds toward four cancer cell lines, namely, colorectal Caco-2, breast MCF-7, cervical HeLa, and liver HepG-2, were evaluated using the MTT assay protocol and using NF and 5-FU as reference compounds. Inhibitory potencies as IC_{50} values are reported in Table 2. For the Caco-2 cell line, all compounds, except **3b**, were more potent

https://doi.org/10.1021/acs.jmedchem.2c01408
J. Med. Chem. 2023, 66, 4565−4587

Table 1. IC_{50} (μM) and EC_{100} (μM) of Synthesized Compounds toward the Human Normal Cell Line (Wi-38)[a]

Cpd ID	IC_{50}	EC_{100}
1	**0.306 ± 0.002**	**0.110 ± 0.002**
2a	0.220 ± 0.005	0.036 ± 0.000
2b	0.150 ± 0.003	0.029 ± 0.004
2c	0.183 ± 0.011	0.026 ± 0.011
2d	0.232 ± 0.006	0.027 ± 0.008
2e	**0.249 ± 0.003**	**0.097 ± 0.002**
2f	0.879 ± 0.016	0.032 ± 0.002
3a	0.216 ± 0.006	0.033 ± 0.000
3b	0.119 ± 0.005	0.032 ± 0.001
3c	0.181 ± 0.000	0.009 ± 0.001
4a	0.226 ± 0.015	0.019 ± 0.002
4b	**0.251 ± 0.009**	**0.098 ± 0.004**
4c	**0.240 ± 0.005**	0.066 ± 0.003
4d	0.180 ± 0.008	0.033 ± 0.001
4e	0.140 ± 0.004	0.026 ± 0.004
NF	0.162 ± 0.011	0.027 ± 0.001
5-FU	0.192 ± 0.003	0.017 ± 0.003

[a]All values were expressed as mean ± SEM (n = 3). Incubation time is 72 h.

than 5-FU while nine derivatives (**1**, **2b**, **2d**−**f**, **3c**, **4a**, **4c**, and **4e**) were either equipotent or more potent than NF. Modification of NF to obtain the propargyl derivative **1** led to enhanced inhibitory potency, showing 1.2 and 2.7 times the activity of NF and 5-FU, respectively. Click modification of **1** into the corresponding 1,2,3-triazoles (**2a**−**f**) led to a variable range of activities; namely, the unsubstituted derivative **2a** showed reduced activity (0.144 vs 0.099 μM for the propargyl derivative), while derivatives bearing EWGs Cl (**2b**), SO_2NH_2 (**2e**), and thiazolyl benzenesulfonamide (**2f**) displayed significant enhanced effects (0.077−0.087 μM). Among the benzyl series **3a**−**c**, the NO_2 derivative (**3c**) was more potent than the unsubstituted benzyl compound (**3a**). Regarding substitution with phenacyl moieties (**4a**−**e**), it was evident that the extra carbonyl function contributed to a significant increase in potency specially with the unsubstituted and Br-substituted derivatives (**4a** and **4c**), when compared to their benzyl congeners **3a**,**b**.

Regarding the MCF-7 cell line, all compounds, apart from **4d**, were superior to 5-FU with IC_{50} values in the range of 0.076−0.198 μM representing 1.2−3.1 fold the activity of the latter. It is worth highlighting that around 10 compounds showed significant *in vitro* antiproliferative activities (0.076−0.117 μM) on this cell line, marking it as the most sensitive and featuring the respective structural modifications as beneficial. Propargylation of NF to yield compound **1** shifted the activity level of the former from inactive to low submicromolar IC_{50} values. The triazoles **2a**−**f** revealed that the unsubstituted **2a** and EWG-substituted derivatives (**2b**,**c**,**e**,**f**) were more potent than the methyl counterpart **2d**. Additionally, the electron-deficient benzyl derivatives **3b**,**c** demonstrated slightly higher activity than the unsubstituted benzyl **3a** bearing in mind that the bromo derivative **3b** showed almost 3 times the activity of 5-FU. Among the phenacyl-appended NF derivatives, the unsubstituted prototype **4a** was found to be the most potent followed by **4b**,**c** and **4d**,**e** bearing EWGs and EDGs, respectively.

Concerning the HeLa cell line, all tested compounds, except **1**, **3b**, and **4a**, showed enhanced activity in comparison to NF and 5-FU. The propargyl derivative **1** was the least potent among the whole series, yet still showing considerable activity with low submicromolar IC_{50} values. Meanwhile, enhancement of the activity was evident upon its click transformation into 1,2,3-triazoles **2a**−**f**. Interestingly, the methyl-substituted counterpart **2d** was the most potent, showing almost twice the activity of the nitro and thiazolyl benzenesulfonamide derivatives **2c**,**f**. For the benzyl subset of compounds, the unsubstituted benzyl **3a** and nitro-substituted **3c** derivatives were almost equipotent (approximately 1.5 times the activity of 5-FU) and showed higher activity than the bromo derivative **3b**. Careful inspection of the structures of the phenacyl derivatives **4a**−**e** revealed that incorporation of either an EW or ED substituent is advantageous as noticed with compounds **4d**,**e** (IC_{50} values in the range of 0.062−0.115 μM).

Regarding the HepG-2 cell line, nine compounds (**1**, **2a**, **2c**, **2f**, **3a**−**c**, **4b**, and **4e**) exhibited higher growth inhibitory activities than 5-FU. They were 1.2−2.8 times more potent

Table 2. IC_{50} (μM) of Different Candidate Compounds against Human Cancer Cell Lines[a]

	Caco-2	SI	MCF-7	SI	HeLa	SI	HepG-2	SI
1	**0.099 ± 0.011**	**3.133 ± 0.36**	**0.111 ± 0.011**	**2.787 ± 0.3**	0.265 ± 0.008	1.155 ± 0.03	**0.089 ± 0.002**	**3.455 ± 0.06**
2a	0.144 ± 0.007	1.53 ± 0.04	0.128 ± 0.013	1.743 ± 0.21	**0.084 ± 0.000**	2.61 ± 0.06	**0.104 ± 0.001**	2.112 ± 0.06
2b	**0.077 ± 0.000**	1.946 ± 0.03	**0.085 ± 0.009**	1.775 ± 0.15	**0.078 ± 0.004**	1.917 ± 0.13	0.400 ± 0.026	0.376 ± 0.03
2c	0.140 ± 0.01	1.316 ± 0.01	**0.117 ± 0.000**	1.565 ± 0.1	**0.113 ± 0.001**	1.621 ± 0.08	**0.063 ± 0.001**	**2.922 ± 0.25**
2d	**0.113 ± 0.007**	2.049 ± 0.08	0.145 ± 0.001	1.596 ± 0.05	**0.059 ± 0.003**	**3.919 ± 0.29**	0.283 ± 0.027	0.824 ± 0.06
2e	**0.080 ± 0.009**	**3.14 ± 0.3**	**0.074 ± 0.002**	**3.359 ± 0.07**	**0.081 ± 0.004**	**3.081 ± 0.18**	0.309 ± 0.014	0.807 ± 0.05
2f	**0.087 ± 0.007**	1.006 ± 0.1	0.120 ± 0.002	0.727 ± 0.12	**0.108 ± 0.001**	0.813 ± 0.15	**0.071 ± 0.002**	1.225 ± 0.19
3a	0.182 ± 0.007	1.187 ± 0.01	**0.113 ± 0.004**	1.916 ± 0.13	0.129 ± 0.002	1.68 ± 0.08	0.120 ± 0.005	1.816 ± 0.13
3b	negative	negative	**0.080 ± 0.005**	1.499 ± 0.04	0.183 ± 0.001	0.65 ± 0.02	**0.067 ± 0.000**	1.784 ± 0.07
3c	**0.103 ± 0.003**	1.752 ± 0.06	**0.103 ± 0.009**	1.772 ± 0.15	0.121 ± 0.009	1.51 ± 0.12	0.127 ± 0.000	1.42 ± 0.002
4a	**0.073 ± 0.003**	**3.075 ± 0.09**	**0.076 ± 0.002**	**2.984 ± 0.29**	negative	negative	0.277 ± 0.018	0.824 ± 0.11
4b	0.134 ± 0.014	1.873 ± 0.09	**0.117 ± 0.000**	2.14 ± 0.07	**0.062 ± 0.003**	**4.044 ± 0.05**	**0.110 ± 0.006**	2.291 ± 0.2
4c	**0.078 ± 0.000**	**3.052 ± 0.05**	**0.105 ± 0.01**	2.315 ± 0.26	0.097 ± 0.002	2.47 ± 0.1	0.289 ± 0.013	0.8305 ± 0.05
4d	0.140 ± 0.015	1.284 ± 0.003	0.255 ± 0.005	0.706 ± 0.02	**0.115 ± 0.008**	1.58 ± 0.17	0.287 ± 0.008	0.628 ± 0.04
4e	**0.105 ± 0.014**	1.366 ± 0.2	0.198 ± 0.007	0.706 ± 0.01	**0.087 ± 0.004**	1.608 ± 0.12	0.149 ± 0.012	0.948 ± 0.1
NF	0.115 ± 0.001	1.408 ± 0.1	negative	negative	0.166 ± 0.005	0.9804 ± 0.09	negative	negative
5-FU	0.266 ± 0.011	0.76 ± 0.01	0.235 ± 0.018	0.865 ± 0.1	0.199 ± 0.006	1.016 ± 0.07	0.178 ± 0.009	1.132 ± 0.02

[a]All values were expressed as mean ± SEM (n = 3). Incubation time is 72 h.

https://doi.org/10.1021/acs.jmedchem.2c01408
J. Med. Chem. 2023, 66, 4565−4587

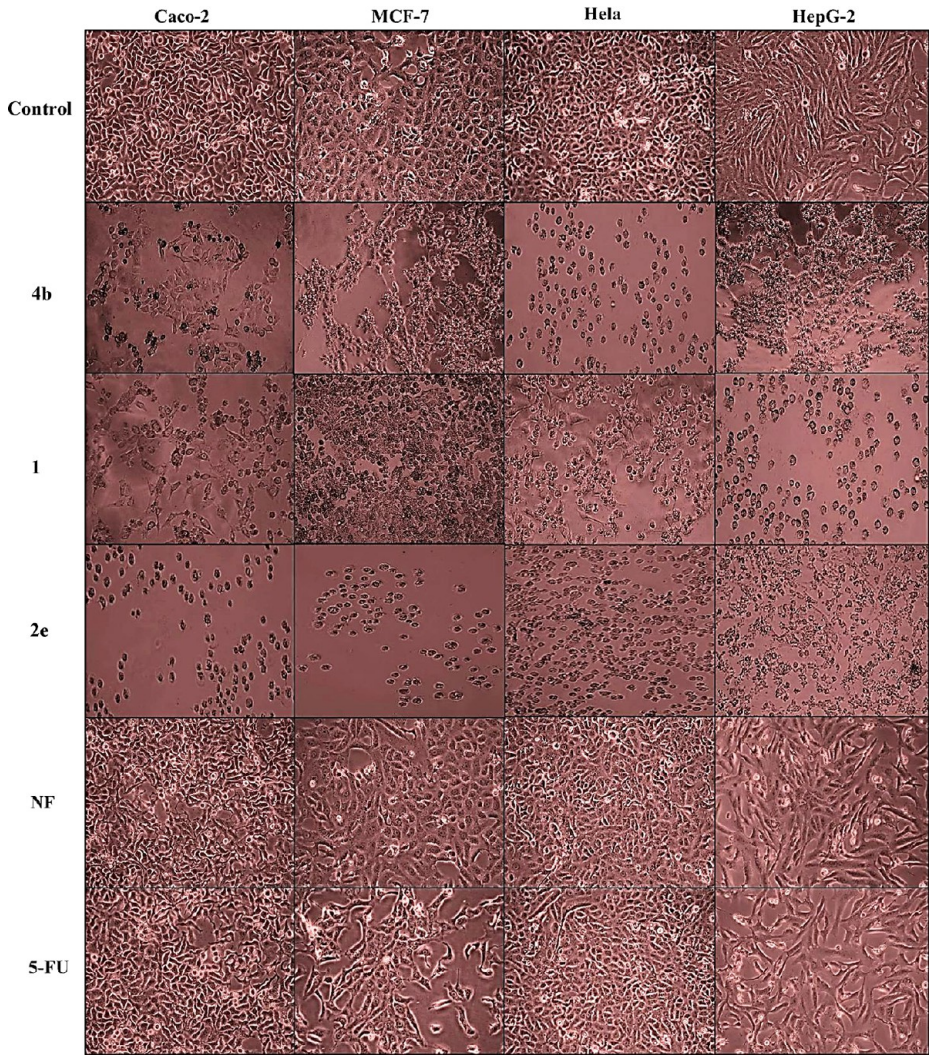

Figure 2. Morphological changes of human cancer cell lines; Caco-2, MCF-7, HeLa, and HepG-2 before and after 72 h treatment with the most active compounds **1**, **2e**, and **4b** compared to NF and 5-FU at their EC_{100}.

(IC_{50} values in the range of 0.063−0.149 μM vs 0.178 μM for 5-FU). In this case, the propargyl derivative **1** regained its potent anticancer activity being two times as active as 5-FU. In the triazole series, the nitro derivative **2c** and the thiazolyl benzenesulfonamide **2f** showed the highest activity and were even 1.4 and 1.25 times more potent than the parent propargyl derivative, respectively. The benzyl subset of compounds exerted significant inhibitory activities with the bromo derivative **3b** being the most active (IC_{50} value 0.067 μM). With respect to the phenacyl series, the chloro **4b** and methoxy **4e** derivatives were the most potent (1.6 and 1.2 times the activity of 5-FU, respectively). On the other hand, the parent phenacyl **4a**, bromo **4c**, and methyl **4d** derivatives showed reduced activity. In comparison to their benzyl congeners **3a** and **3b**, the insertion of the carbonyl function in **4a** and **4c** was detrimental to anticancer activity.

Briefly, it can be roughly concluded that electron-deficient substituents on all of the three employed aromatic motifs favored improved activity and selectivity. In addition, the propargyl derivative demonstrated an outstanding anticancer profile, which is a solid proof of its pharmacophoric importance as we previously reported for other bioactive compounds in different biological contexts.[29,30]

Therefore, this study represents a good foundation for future in-depth investigations in the field of chemotherapy by attempting more diverse arrays of molecular frameworks with various substitution patterns grafted on the promising NF scaffold.

The selectivity index (SI) of an anticancer agent is the ratio between IC50 of the compound on normal cells and its IC50 value on cancerous cells. It gauges the capability of the drug candidate to discriminate between cancer and normal cells.[31] Compounds are highly selective when they exhibit SI values of more than 3.[32]

Selectivity indices recorded in Table 2 indicated the selectivity of the propargyl derivative (**1**) with SI values of 2.8, 3.1, and 3.5 against MCF-7, Caco-2, and HepG-2 cell lines, respectively. Within the triazole series, compound **2c** was the most selective against the HepG-2 cell line while **2d** showed a high SI of 3.9 against the HeLa cell line. Also, compound **2e** demonstrated high selectivity for three cancer cell lines, namely, Caco-2 (3.1), MCF-7 (3.4), and HeLa (3.1). Among the phenacyl substituted NF derivatives, compound **4a** showed high selectivity indices toward Caco-2 (3.1) and MCF-7 (3) cell lines. As well, compound **4b** showed high selectivity index toward the HeLa cell line and **4c** was the most selective for the Caco-2 cell line.

https://doi.org/10.1021/acs.jmedchem.2c01408
J. Med. Chem. 2023, 66, 4565−4587

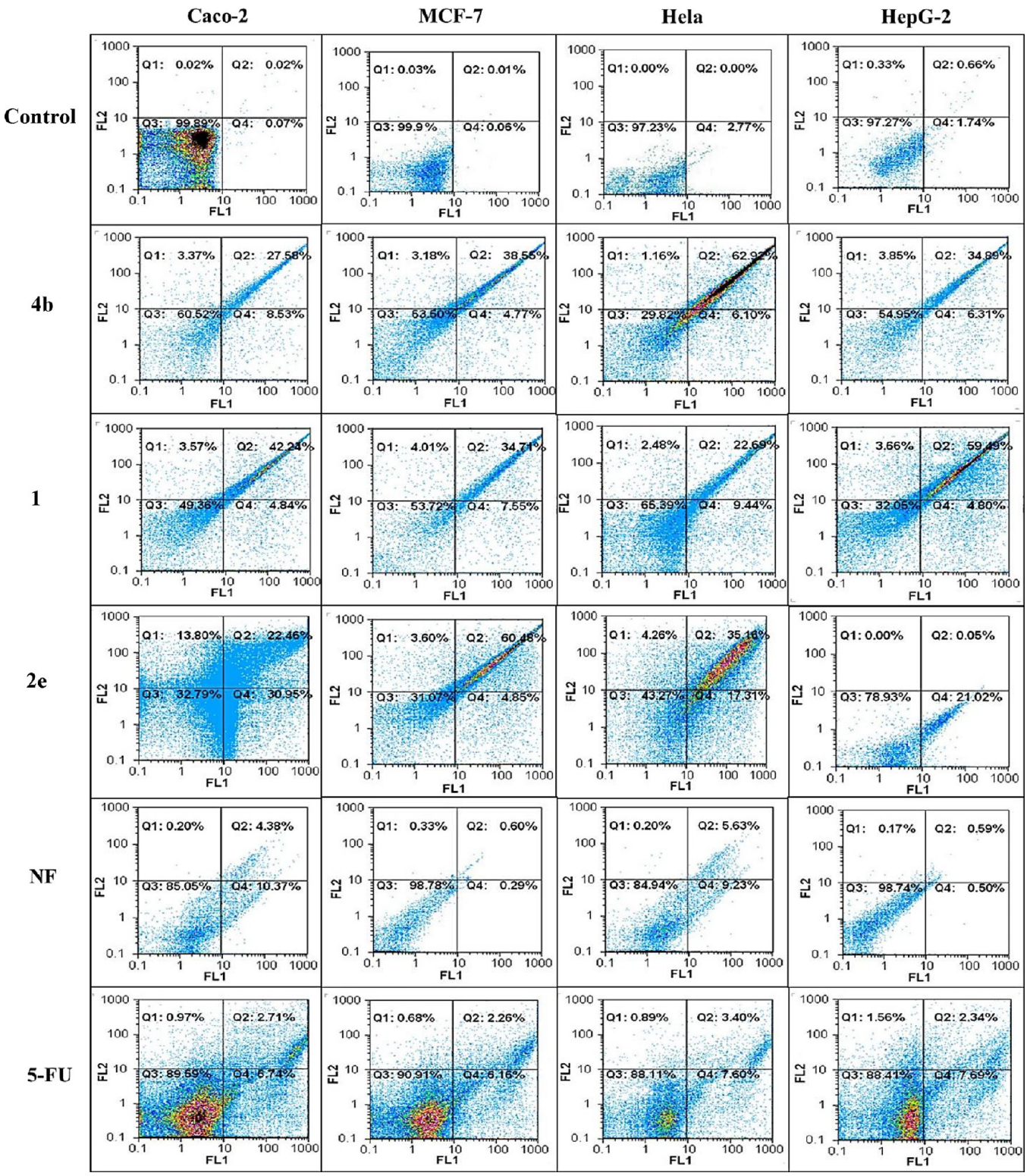

Figure 3. Annexin-PI analysis of human cancer cell lines; Caco-2, MCF-7, HeLa, and HepG-2 before and after 72 h treatment with the most active compounds **1**, **2e**, and **4b** compared to NF and 5-FU at their EC_{100}.

2.2.3. Analysis of Morphological Changes. Cellular morphological changes before and after 72 h treatment with the most active compounds **1**, **2e**, and **4b**, compared to NF and 5-FU, were investigated using a phase contrast inverted microscope with a digital camera (Olympus, Japan).

It was found that untreated cancer cells preserved their original morphology. On the other hand, cells treated with compounds **1**, **2e**, and **4b**, compared to the control cells, appeared smaller, rounded, and losing contact with neighboring cells. Shrinkage and absence of the normal spindle shape were also observed, as shown in Figure 2. This is suggestive of programmed cell death as designated in some reports.[33]

2.2.4. Repurposed Nitrofurantoin Derivative-Evoked Human Cancer Cell Line Cytotoxicity Proceeds through

https://doi.org/10.1021/acs.jmedchem.2c01408
J. Med. Chem. 2023, 66, 4565−4587

Table 3. Percentage of Apoptotic Cells before and after Treatment of Different Cancer Cell Lines[a]

	Caco-2	MCF-7	HeLa	HepG-2
control	0.04 ± 0.005[e]	0.04 ± 0[d]	0 ± 0.035[f]	0.99 ± 0.02[e]
1	45.81 ± 0.17[b]	38.72 ± 0.14[b]	25.17 ± 0.045[c]	**63.15 ± 0.05**[a]
2e	36.26 ± 4.5[a]	**64.08 ± 0.12**[a]	39.42 ± 0.06[b]	0.05 ± 0.035[c]
4b	30.95 ± 0.09[c]	41.73 ± 0.05[b]	**64.08 ± 0.05**[a]	38.74 ± 0.2[b]
NF	4.58 ± 0.07[d]	0.93 ± 0.05[d]	5.83 ± 0.03[e]	0.76 ± 0.05[e]
5-FU	3.68 ± 0.03[d]	2.94 ± 0.028[c]	4.29 ± 0.04[d]	3.9 ± 0.025[d]

[a]All values were expressed as mean ± SEM. Different letters for the same column were significantly different at $p < 0.05$ using one-way ANOVA followed by Tukey's *post hoc* test.

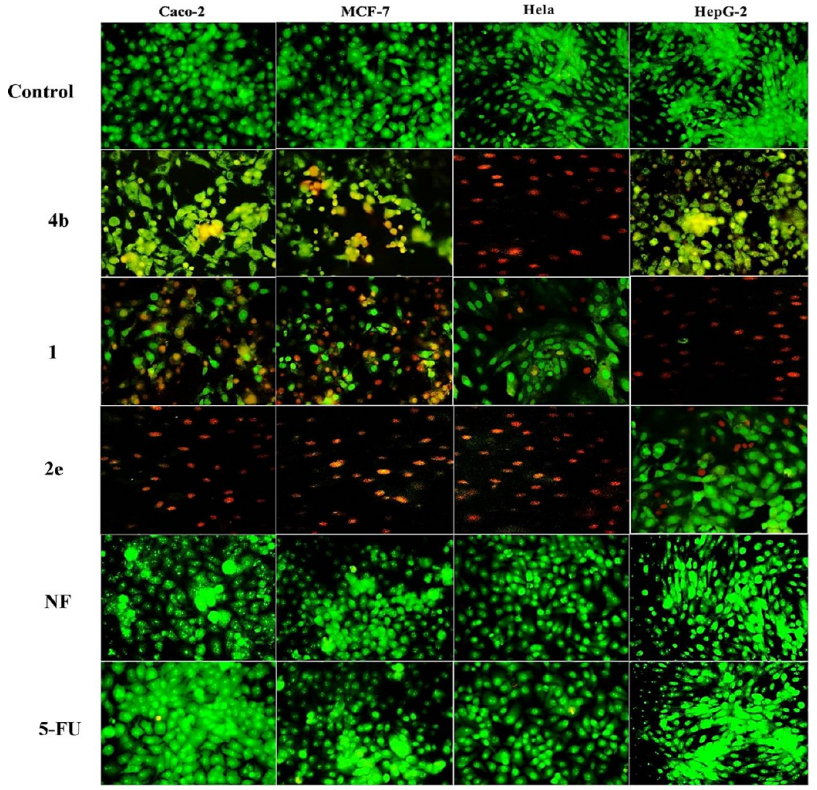

Figure 4. AO-EB double staining of cells in different stages of apoptosis visualized using fluorescence microscopy for human cancer cell lines; Caco-2, MCF-7, HeLa, and HepG-2 before and after 72 h treatment with the most effective safe anticancer compounds compared to NF and 5-FU at their EC_{100}.

Induction of Apoptosis. To ascertain the apoptotic capability of compounds **1**, **2e**, and **4b** in the previously tested cancer cell lines, the annexin V-FITC/propidium iodide dual staining assay was performed (Figure 3 and Table 3). This analysis indicated that compound **1** triggered an appreciable increase in the percentage of annexin V-positive apoptotic population of 45.81%, 38.72%, and 25.17% in Caco-2, MCF-7, and HeLa cells, respectively. As for the HepG-2 cell line, compound **1** showed significant apoptotic potential by 63.15%.

Also, the percentages of annexin V positive apoptotic cells produced by compound **2e** were 36.26% and 39.42% in Caco-2 and HeLa cells, respectively. In addition, the MCF-7 cell line demonstrated the highest percentage of annexin V-positive apoptotic cells (64%). It almost showed no apoptosis in HepG-2 cells. Upon treatment with compound **4b**, the percentages of annexin V positive apoptotic cells were 31%, 42%, 64%, and 39% for Caco-2, MCF-7, HeLa, and HepG-2 cells, respectively and hence confirming cell death by apoptosis. It is worth mentioning that NF and 5-FU displayed 0.76−5.83% of the total apoptotic cells in the four cell lines.

Induction of apoptosis was further substantiated by employing fluorescence microscopy after acridine orange (AO) and ethidium bromide (EB) dual staining of cancer cell lines. Based on the fluorescence emission and the morphology of chromatin condensation in the nucleus, cells are considered viable if they are green and highly organized.[34,35] Early apoptotic cells (with intact membranes so EB cannot get into the cell, but DNA fragmentation was started) appear as patches with bright green color. Meanwhile, late apoptotic cells show orange to red fluorescing nuclei together with fragmented or condensed chromatin that can differentiate these cells from necrotic cells, which are stained orange in a uniform manner.[34,35] As shown in Figure 4, it was not surprising that all four tested cancer cell lines, treated with the most active compounds **1**, **2e**, and **4b**, displayed either bright green patches, orange, or orange red colors, thereby confirming apoptosis. On the other hand, NF- and 5-FU-treated cells appeared visibly green and uniform.

2.2.5. Determination of Redox Alteration in Cancer Cells by Flow Cytometry. At this point, we attempted to provide further insight into the molecular mechanism through which these

https://doi.org/10.1021/acs.jmedchem.2c01408
J. Med. Chem. 2023, 66, 4565−4587

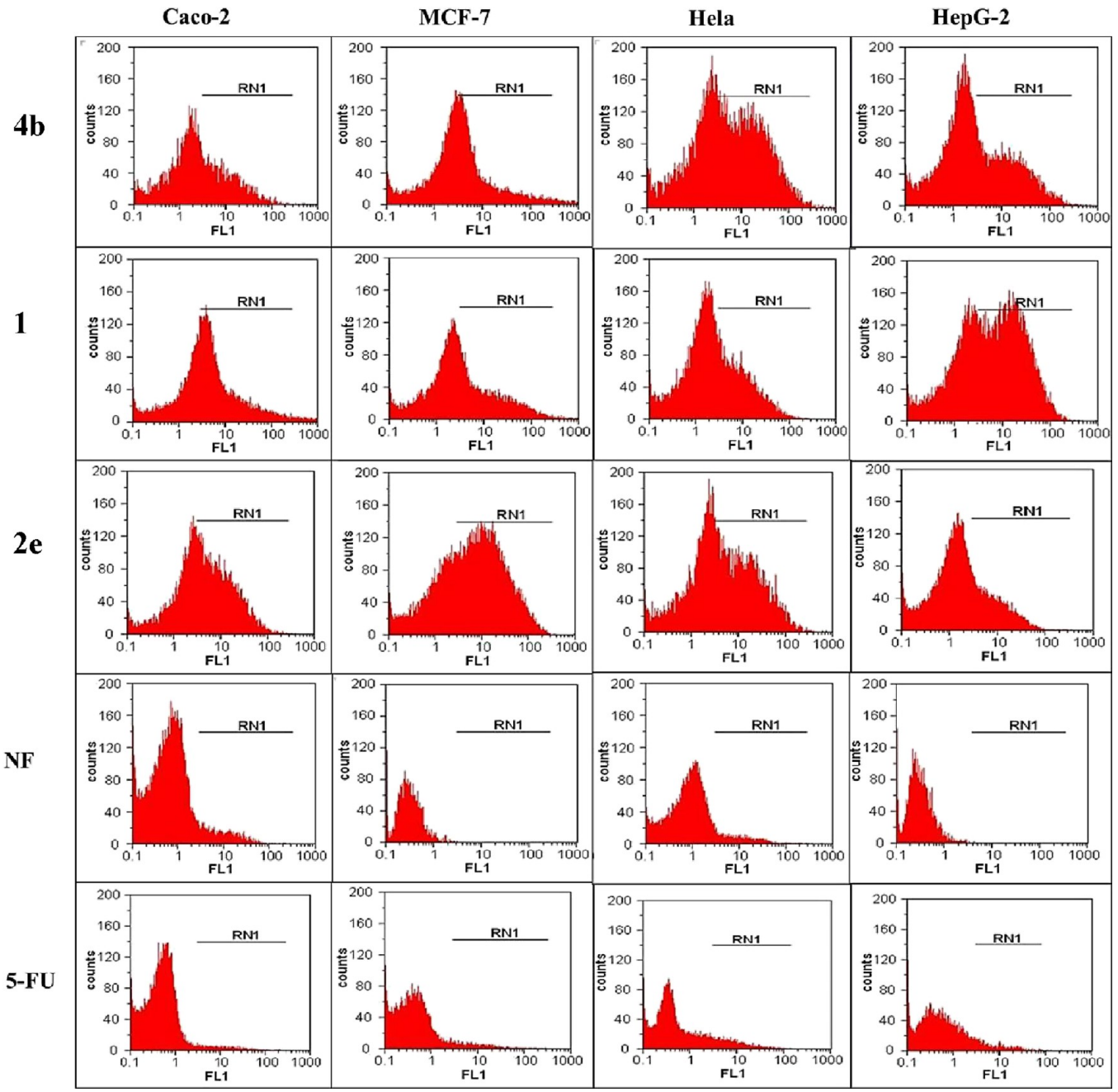

Figure 5. Flow cytometric analysis of relative DCFH-DA oxidation in human cancer cell lines; Caco-2, MCF-7, HeLa, and HepG-2 after 72 h treatment with the most active compounds **1**, **2e**, and **4b** compared to NF and 5-FU at their EC_{100}.

Table 4. Increment Percentage in DCFH-DA Oxidation in Human Cancer Cell Lines after Treatment with the Most Active Compounds[a]

	Caco-2	MCF-7	HeLa	HepG-2
1	45.56 ± 0.38^{b}	35.5 ± 0.71^{c}	30.75 ± 0.66^{c}	54.19 ± 0.9^{a}
2e	51.08 ± 0.08^{a}	53.5 ± 0.71^{a}	48.51 ± 1.11^{b}	22.21 ± 1.17^{c}
4b	32.41 ± 0.64^{c}	38.99 ± 0.17^{b}	54.7 ± 0.3^{a}	34.7 ± 0.57^{b}
NF	8.43 ± 0.13^{d}	0 ± 0^{e}	7.61 ± 0.11^{d}	0 ± 0^{e}
5-FU	4.78 ± 0.04^{e}	4.24 ± 0.025^{d}	4.91 ± 0.04^{d}	4.78 ± 0.03^{d}

[a]All values were expressed as mean ± SEM. Different letters for the same column were significantly different at $p < 0.05$ using one-way ANOVA followed by Tukey's *post hoc* test.

compounds induced apoptotic cell death. Indeed, the oxidative stress resulting from the reduction of the nitro group in the nitrofuran structure forms the basis of its DNA damaging effect in eukaryotic cells.[36] To explore the oxidative load evoked by the current compound series in different cancer cell lines, dihydrodichlorofluorescein diacetate (DCFH-DA) was used to

https://doi.org/10.1021/acs.jmedchem.2c01408
J. Med. Chem. 2023, 66, 4565−4587

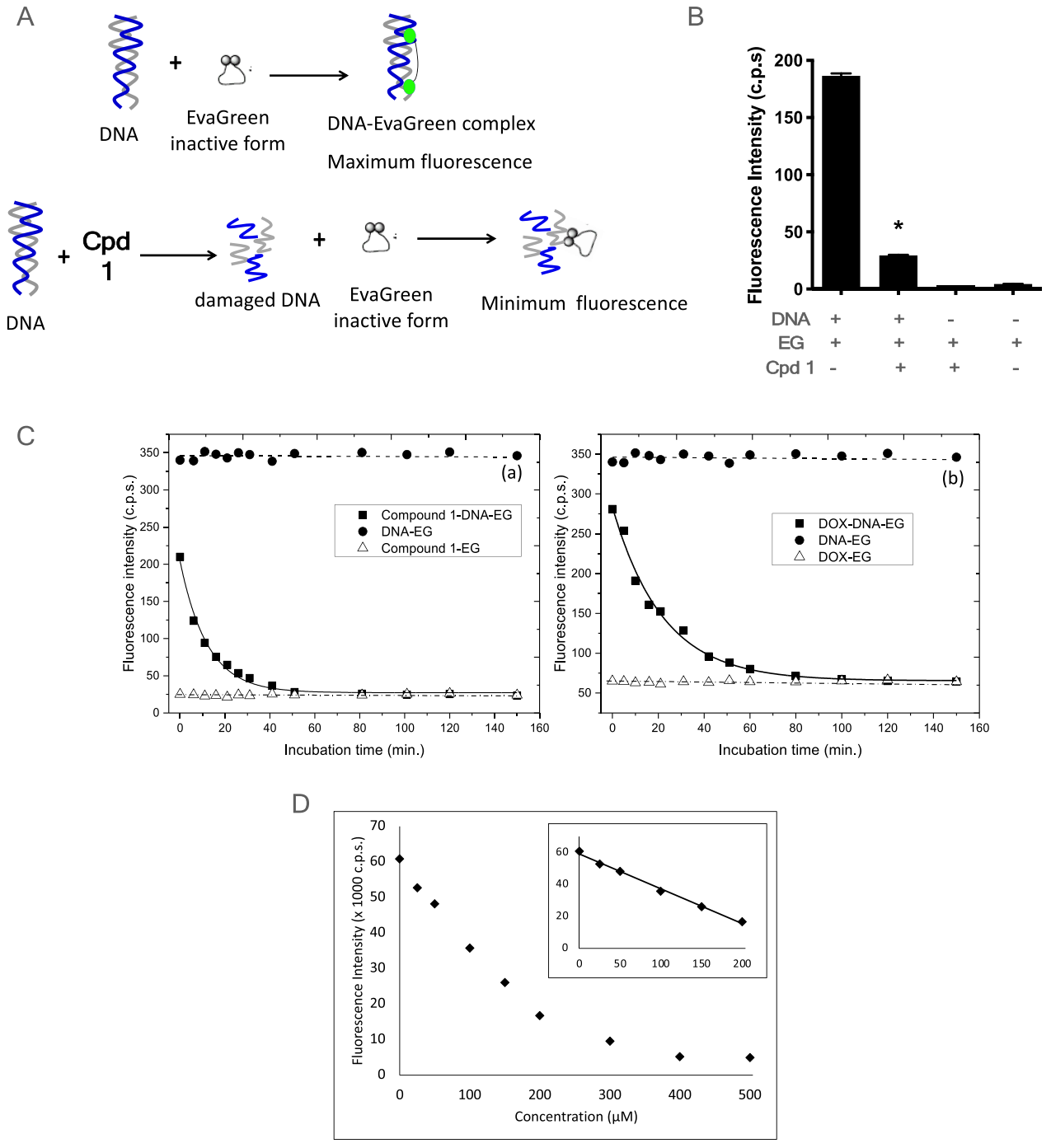

Figure 6. Fluorimetric detection of DNA damage extent and kinetics using the EvaGreen (EG) biosensor. (A) Schematic diagram for the assay; (B) fluorescence intensity at 530 nm of the DNA-EG complex in the presence and absence of compound **1** after excitation at 490 nm. Solutions of EG alone and in the presence of compound **1** are experimental controls. The asterisk (*) denotes $P < 0.05$ vs (DNA + EG) using one-way ANOVA followed by Dunett's *post hoc* test; (C) EG fluorescence intensity in cps (counts per second) of the dsDNA-EG complex as a function of incubation time with (a) Cpd **1** and (b) DOX (black squares, solid line). EG fluorescence of the DNA alone (black circles, dashed line) and drug alone (white triangles, dashed dotted line) are also shown; (D) fluorescence intensity of the EG-ctDNA-Cpd **1** mixture as a function of Cpd **1** concentration. The inset shows the fit to the linear interval of the curve. The excitation wavelength is 490 nm, and the emission wavelength is 530 nm.

probe the intracellular ROS alterations caused by the most active compounds (**1**, **2e**, and **4b** compared to NF and 5-FU) by using flow cytometric analysis.[37]

As shown in Figure 5 and Table 4, the increment in DCFH-DA oxidation due to prooxidant effects of NF derivatives and generation of ROS was above 50% in **4b**-treated HeLa cells, **1**-treated HepG-2, and **2e**-treated Caco-2 and MCF-7 cell lines. This indicated a severe oxidative redox state of the treated cancer cells compared to untreated and NF- or 5-FU-treated ones (<8.5%). Hence, the cells became more susceptible to oxidative stress-induced cell death.

2.2.6. DNA Binding and Direct DNA Damage Studies. Afterward, we sought to obtain a quantitative measure of the direct DNA damaging effects of these compounds. This was carried out using the EvaGreen (EG) fluorescent biosensor[38] to study the possible DNA interaction with compound **1** as shown

https://doi.org/10.1021/acs.jmedchem.2c01408
J. Med. Chem. 2023, 66, 4565−4587

in Figure 6A. Results depicted in Figure 6B showed enhanced EG fluorescence for the dsDNA solution alone. This indicates that the dsDNA was intact without any disruption in the DNA double helical structure. Meanwhile, a significant decrease in EG fluorescence was observed upon addition of compound **1** to DNA. This reflects the DNA damage induced by such a compound, where EG was detached from the damaged DNA acquiring the closed loop conformation with minimum fluorescence intensity. On the other hand, controls, such as the compound **1**-EG mixture and EG solution alone, showed almost no fluorescence. This confirms that, in the absence of DNA, EG acquired the closed loop conformation and there were no interferences from the reaction matrix. To further explore whether the decrease in EG fluorescent intensity associated with the addition of compound **1** is correlated to the amount of damage produced, the kinetics of compound **1**-dsDNA interaction were studied by measuring the change in EG fluorescence of DNA-EG- compound **1** solution over time. In order to ensure that the change in EG fluorescence was due to the effect of compound **1** on DNA, the obtained data were compared to those of DNA-EG and compound **1**-EG solutions. The results obtained are shown in Figure 6C. The fluorescence intensity of DNA-EG solution in the absence of compound **1** remained constant at high fluorescence levels throughout the entire measurement period. This confirms the complete intercalation of EG within the intact DNA. Meanwhile, in the presence of compound **1**, the fluorescence intensity decreased gradually and exponentially with increasing incubation time until the fluorescence reached its minimum intensity after ∼50 min of incubation. This gradual decrease in fluorescence with time was interpreted as compound **1**-induced DNA damage, which led to decomplexation of EG from the DNA with a consequent decrease in fluorescence emission. After 50 min of incubation, the fluorescence intensity of the DNA-EG-compound **1** mixture remained constant and overlapped the compound **1**-EG fluorescence plot until the end of the measurements, which indicates that EG was completely released. It is noteworthy that the fluorescence intensity of the compound **1**-EG sample remained essentially constant throughout the measurement showing minimal fluorescence that did not change with incubation time.

In order to further examine DNA damage induced by the studied molecule, the compound **1**-DNA damage kinetics (Figure 6C) were compared to the DNA damage kinetics induced by doxorubicin (DOX), a widely used anticancer chemotherapeutic agent that induces DNA damage as its main anticancer mechanism.[39] Initial assessment of the two damage plots shows that EG fluorescence of compound **1**-DNA-EG solution measured directly after the addition of compound **1** (at 0 min) is lower than that of DOX-DNA-EG. This indicates that the studied compound causes more instantaneous disruption of the DNA helical structure than DOX, *i.e.*, causing more damage. Moreover, in order to obtain a clear comparison of the effect of compound **1** and DOX on DNA, the rate of decrease in EG fluorescence of the DNA-EG solution in the presence of either compound was calculated by fitting data points obtained in Figure 6C to a single exponential function: $I_F = I_{F0} + Ae^{-t/\tau}$, where I_F is the fluorescence intensity at time t, I_{F0} is the fluorescence intensity at time 0, A is the amplitude, and $e^{-t/\tau}$ is the exponential decay with τ representing the damage constant. The decrease in EG fluorescence indicates the decrease in stability of the damaged DNA. Thus, the faster the fluorescence decreases, the faster is the rate of damage and the smaller is the damage constant (τ). Table 5 illustrates the damage constants acquired by fitting the fluorescence damage curves for both compound **1** and DOX, clearly showing that the DNA damage kinetics of compound **1** were twice as fast as DOX with $\tau_{Cpd\ 1}$ being almost half of τ_{DOX}. This indicated that compound **1** has a more potent DNA damaging effect than DOX.

Table 5. Kinetic Parameters of DNA Damage Induced by Compound 1 and DOX

damage kinetics parameters	Cpd **1**-DNA	DOX-DNA
$I_{F,0}$	27.22 ± 2.44	65.36 ± 3.98
A	176.74 ± 5.61	218.11 ± 6.71
τ	8.41 ± 0.54	15.23 ± 1.14

Therefore, in order to study the potency of compound **1**-induced DNA damage, the effect of such a compound was studied on calf thymus DNA (ctDNA), a natural DNA extracted from the thymus gland of a calf. Different concentrations (0−500 μM) of compound **1** was mixed with ctDNA-EG, separately. Figure 6D demonstrates the concentration-dependent reduction in EG fluorescence, which peaks at 200 μM concentration of compound **1**. Table 6 demonstrates the quantification parameters of compound **1**-induced DNA damage calculated from data points in Figure 6D. The inset presents the linear interval of the plot. The linearity of the results was established to deduce the minimum concentration of compound **1** that induces DNA damage (LOD). Results showed that a concentration as low as 3.25 nM compound **1** is sufficient to induce a detectable damage in ctDNA (Table 6), which indicates the significant potency of compound **1** as a DNA damaging agent.

Table 6. Analytical Parameters of EG Fluorescence Measurements of Cpd 1−ctDNA Mixtures

parameter	Cpd **1**
linear dynamic range (μM)	0.01−200
correlation coefficient (r)	0.9945
intercept (a)	59.13×10^3
slope (b)	-21.81×10^3
LOD[a] (nM)	3.25
LOQ[b] (nM)	10.80

[a]LOD: limit of detection, which is 3.3 times the standard deviation of the blank divided by the slope. [b]LOQ: limit of quantification, which is 3.3 times the LOD.

2.2.7. Assessment of Early Cellular Response to DNA Damage and p53 Dependence of Cell Death. As the EG DNA damage assay indicated a very rapid DNA damaging effect of compound **1**, we proceeded to examine whether cancer cells demonstrated a DNA damage response in a time frame that is shorter than that used for the cytotoxicity studies (24 vs 72 h). As mentioned in the Introduction, following double stranded DNA breaks, phosphorylated ATM is shuttled to the nucleus followed by p53 activation and initiation of the apoptotic sequence. Toward this end, different concentrations of the most active compounds (**1**, **2e**, and **4b**) as well as NF were incubated with MCF-7, Caco-2, and Hep-G2 cells for 24 h and cell viability was assessed by the MTT assay. As expected, IC_{50} values measured were much higher than those observed after 72 h of incubation (Figure 7A). However, compound **1** consistently showed the lowest IC_{50} values toward MCF-7, Caco-2, and

https://doi.org/10.1021/acs.jmedchem.2c01408
J. Med. Chem. 2023, 66, 4565−4587

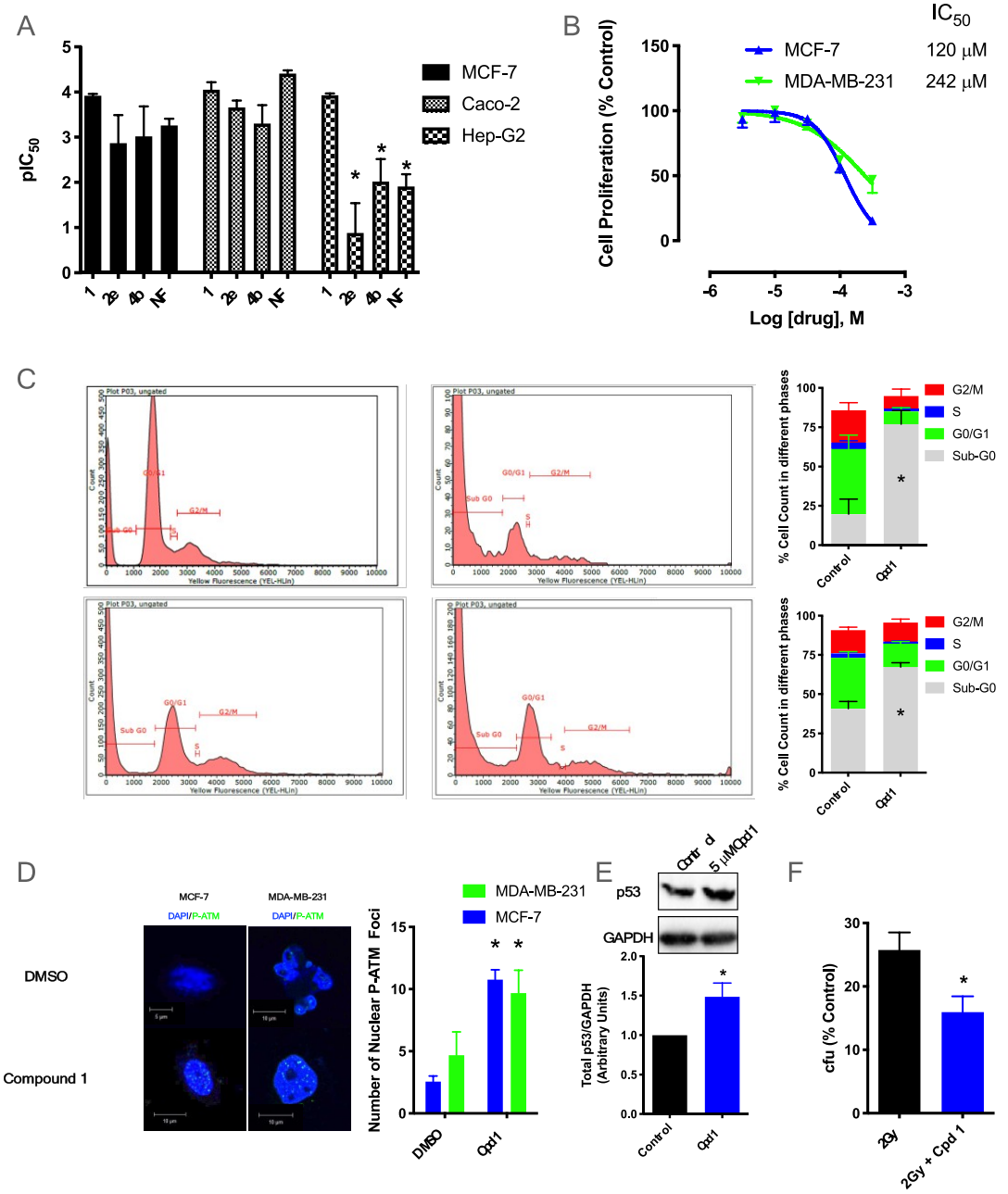

Figure 7. Early cellular response to the DNA damaging effect of nitrofurantoin derivatives. (A) pIC_{50} ($-\log IC_{50}$) of the four most active candidates after a 24 h incubation period with different cell lines; (B) concentration dependence of the cytotoxic effect of Cpd **1** against MCF-7 and MDA-MB-231 cells; (C) Cell cycle analysis of MCF-7 and MDA-MB-231 cells after a 24 h incubation period with and without Cpd **1**. Bar graphs (right) depict the percentage of cells in different phases; (D) fluorescent micrographs showing P-ATM shuttling in MCF-7 and MDA-MB-231 cells after a 4 h incubation period with and without Cpd **1**. Data are summarized in the bar graph; (E) western blotting analysis of the p53 expression level in MCF-7 cells after a 24 h incubation period with and without Cpd **1**; (F) decrease in radiosensitive UC3 cell colony formation potential following exposure to radiation in the presence and absence of Cpd **1**. Results are represented as mean ± SEM of three independent experiments. The asterisk (*) denotes *P* value <0.05 using two-way ANOVA followed by Sidak's multiple comparisons test for panel (A) (vs Cpd **1**), (C) and (D) (vs vehicle control), and unpaired *t* test for panels (E) and (F) (vs vehicle control).

HepG-2 cell lines (120, 89, and 117 μM, respectively). As such, compound **1** was selected for further investigation of the early effects leading to cell death. To address the p53 dependence of the cytotoxic effect of this compound series, the 24 h IC_{50} of compound **1** on MCF-7 cells was compared to that on MDA-MB-231 cells, another breast cancer cell line that are triple negative for hormone receptors and elicit a p53 mutation that contributes to cell survival.[40] Interestingly, compound **1** showed a two-fold increase in the 24 h IC_{50} against MDA-MB-231 cells (242 μM) (Figure 7B). Indeed, treatment of MCF-7 and MDA-MB-231 cells with compound **1** at the respective IC_{50} for 24 h followed by cell cycle analysis showed a greater increase in the proportion of apoptotic MCF-7 cells as indicated by the number of cells in the Sub-G0/G1 phase (Figure 7C). However, the P-ATM shuttling response 4 h following the exposure to a concentration equivalent to IC_{50} of compound **1** was similar in both cell types (Figure 7D), indicating that the observed

https://doi.org/10.1021/acs.jmedchem.2c01408
J. Med. Chem. 2023, 66, 4565−4587

difference was not related to the DNA damaging potential, but rather related to the p53 activity.

Therefore, since MDM2 is a master regulator of p53 activity and the literature reported some compounds to be potent MDM2−p53 interaction inhibitors,[26] it became prudent to test our most active compounds **1**, **2e**, and **4b** along with NF for their inhibitory activities toward MDM2−53 interaction. Data recorded in Table 7 revealed that NF itself inhibited MDM2−p53 interaction with an IC_{50} value of 1.58 μM while the three most active NF derivatives **1** (propargyl), **2e** (1,2,3-triazole benzenesulfonamide), and **4b** (4-chloro phenacyl) showed submicromolar IC_{50} values. They were more potent than NF, displaying 2.7, 3.6, and 2.4 times its activity, respectively. These results were confirmed on MCF-7 cells incubated for 24 h with 5 μM of compound **1** for 24 h (10× the IC_{50} for MDM2/p53 interaction and 20× less than the IC_{50} for viability in 24 h). As expected, the presumed reduction of p53 ubiquitination and degradation following the inhibition of MDM2/p53 interaction led to increased p53 expression in treated cells (Figure 7E). Taken together, our data indicate that our compound series not only induce apoptotic cell death by virtue of the classical DNA damaging effect but also through the increased availability of p53 possibly via inhibiting its interaction with MDM2. Further theoretical evidence to support our claim of interference of these compounds with p53−MDM2 interaction was provided by docking simulations (*vide infra* Section 2.3).

Table 7. *In Vitro* p53−MDM2 Interaction IC50 Values of the Most Active Compounds[a]

Cpd ID	IC_{50} (μM)
1	0.59
2e	0.41
4b	0.67
NF	1.58

[a]All values are expressed as the mean of three replicates with standard deviation less than 10% of the mean.

To further contextualize the impact of these compounds as p53 sensitizers, we envisioned that a short exposure (24 h) to a concentration that was shown to increase p53 expression (5 μM), yet two orders of magnitude less than the IC_{50} value for this exposure time and thus presumably producing minimal damage *in cellulo*, should increase the sensitivity of cancer cells to the cytotoxic effects of other DNA damaging signals. Toward this end, we performed a clonogenic assay on the radiosensitive prostatic cancer UC3 cell line after exposure to a 2 Gy dose of ionizing radiation in the presence and absence of 5 μM of compound **1**. As shown in Figure 7F, the ability of irradiated cells to form colonies decreased by about 75% compared to controls. Exposure of UC3 cells to compound **1** further decreased their colony forming ability. Interestingly, the change in clonogenic potential was analogous to the magnitude of increase in p53 expression (1.5×). This observation is of particular importance as it proposes a niche for the use of these compounds to attain significant tumor death with a potentially limited side effect profile. In such a context, a low dose of one of these candidates that is fairly nontoxic to normal body cells would enhance the cytotoxic effect of localized exposure to a limited dose of ionizing radiation.

2.2.8. Effect on the Expression Levels of Mitochondrial Apoptotic Markers Bax and Bcl-2. Following p53 activation, apoptosis proceeds through increased mitochondrial membrane permeability either as a direct effect of p53[41] or as a consequence of altered expression levels of the pro-apoptotic (Bax) and anti-apoptotic (Bcl-2) proteins, both being transcriptional p53 targets.[42] The balance between Bcl-2 and Bax gene expression is important for apoptosis induction.[43] Hence, the association between Bax and Bcl-2 expression may aid in gauging the anticancer potential of a compound.

As shown in Figure 8, the three test compounds upregulated the expression level of Bax in all 4 tested cancer cell lines,

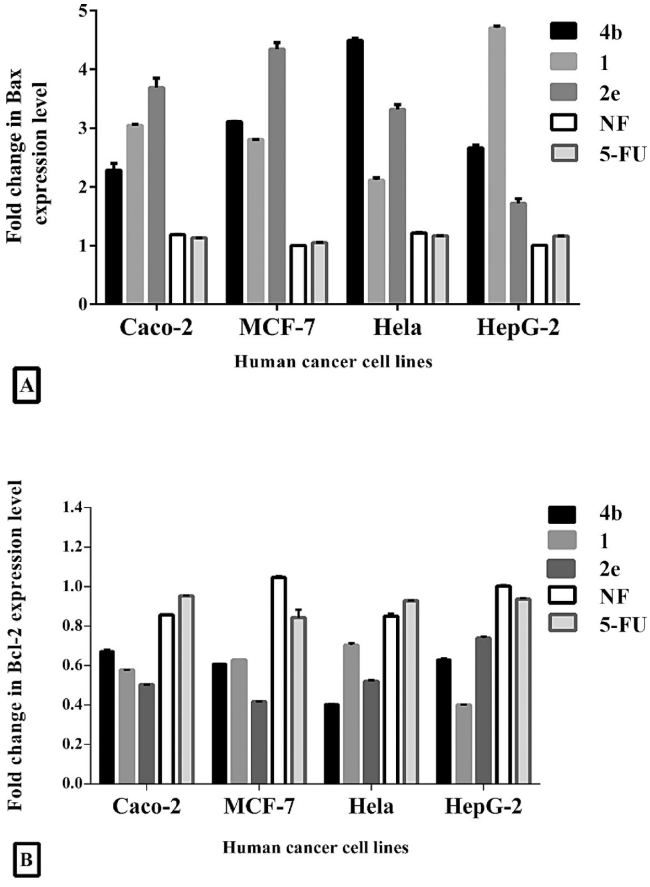

Figure 8. Fold change of Bax (A) and Bcl-2 (B) expression levels in treated cancer cell lines.

showing a 70−350% increase compared to both reference drugs NF and 5-FU. The highest levels, around a 300−400% increase, were recorded for Caco-2 and MCF-7 when exposed to compound **2e** and for HeLa and HepG-2 cell lines upon treatment with compounds **4b** and **1**, respectively. On the other hand, the three compounds afforded significant reduction in Bcl-2 levels producing fold changes in the range of 30−60%, in the four cancer cell lines, in comparison to changes caused by NF and 5-FU. Again, the lowest percentage changes in Bcl-2 levels (50−60%), denoting increased apoptotic propensity, followed the same pattern as observed for Bax upregulation regarding the respective cell line and test compound (Figure 8). Additionally, the Bax/Bcl-2 ratio can function as a rheostat that determines the likelihood of a cell for apoptosis.[44] Table 8 shows a significant increase in the Bax/Bcl-2 ratio (more than 7-fold) in **2e**-treated Caco-2, **2e**-treated MCF-7, **4b**-treated HeLa cells, and **1**-treated HepG-2 when compared to other cancer cell lines. These high ratios indicated that they were more prone to apoptosis than other treated cancer cells. Yet, Bax/Bcl-2 ratios in

https://doi.org/10.1021/acs.jmedchem.2c01408
J. Med. Chem. 2023, 66, 4565−4587

Table 8. Ratio of Pro-apoptotic (Bax)/Anti-apoptotic (Bcl-2) Gene Expression in Treated Cancer Cells[a]

Bax/Bcl-2	Caco-2	MCF-7	HeLa	HepG-2
1	5.278 ± 0.024[b]	4.453 ± 0.003[c]	3.004 ± 0.105[c]	**11.74 ± 0.067**[a]
2e	**7.328 ± 0.355**[a]	**10.4 ± 0.201**[a]	6.36 ± 0.22[b]	2.326 ± 0.139[c]
4b	3.396 ± 0.205[c]	5.104 ± 0.001[b]	**11.09 ± 0.102**[a]	4.215 ± 0.11[b]
NF	1.385 ± 0.006[d]	0.958 ± 0.005[d]	1.42 ± 0.034[d]	1.002 ± 0.0005[d]
5-Fu	1.187 ± 0.004[d]	1.246 ± 0.058[d]	1.257 ± 0.001[d]	1.247 ± 0.007[d]

[a]All values were expressed as mean ± SEM. Different letters for the same column were significantly different at $p < 0.05$ using one-way ANOVA followed by Tukey's *post hoc* test.

the other cell lines (2.3−6.4) were still superior to those recoded for NF and 5-FU (around 1).

2.2.9. Determination of Caspase-Glo 3/7 Activation. In the apoptotic cell death sequence, increased mitochondrial permeability is followed by activation of caspases. These are protease enzymes that play a vital role in programmed cell death. They are required for apoptosis initiation and execution as well as the processing and development of inflammatory cytokines.[45] The apoptosis signal is initiated by initiator caspases, whereas executioner caspases (such as caspases 3 and 7) undertake the mass proteolysis that results in apoptosis.[45] Caspase 3 regulates DNA fragmentation and morphologic alterations during apoptosis, whereas caspase 7 has little influence on these processes. In contrast, caspase 7 seems to be more significant to the loss of cellular viability, albeit both caspases play key roles in this area.[46]

In order to gain a better understanding of how the most active compounds trigger apoptosis, caspases 3 and 7 activities were quantified in cancer cell lines (Caco-2, MCF-7, HeLa, and HepG-2) after exposure to the safe doses (EC_{100}) of compounds **1**, **2e**, and **4b** along with NF and 5-FU for 72 h. Data presented in Figure 9 revealed that compound **1** prompted caspase 3/7

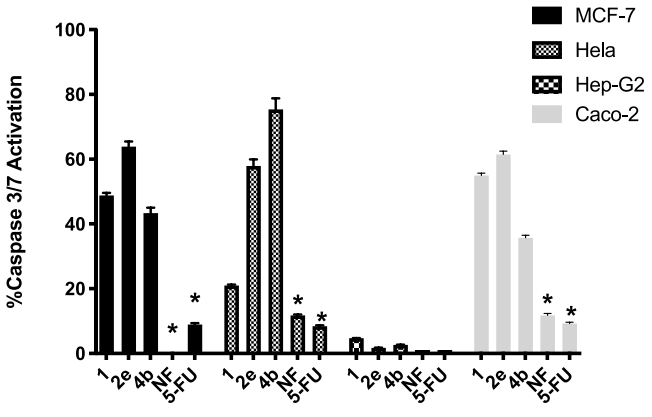

Figure 9. Percentage increase in caspase 3/7 activation in treated cancer cells. The asterisk (*) denotes a *P* value <0.05 vs Cpd **1** for the same cell line using two-way ANOVA followed by Sidak's multiple comparison test.

activation by 55% and 63% in Caco-2 and HepG-2 cells. Moreover, Caco-2, MCF-7, and HeLa cells demonstrated 58−64% caspase 3/7 activities upon treatment with compound **2e**. Meanwhile, compound **4b**-treated HeLa cells were the most sensitive by showing 75% caspase 3/7 activities. These results were significantly higher than caspase activities brought about by NF and 5-FU (maximum 12% activation).

2.2.10. Correlation between Prooxidant Effect and Apoptosis. In order to demonstrate that the different proposed aspects of the cytotoxic mechanisms of our compound series are tightly related, we examined the correlation between the presumed first step of oxidative load production leading to DNA damage and the final manifestation of apoptotic cell death markers. The ratio of Bax/Bcl-2 together with the percentage of annexin-stained apoptotic cells increased with DCFH-DA oxidation percentage in a dose-dependent manner. The high correlation ($r > 0.9$, $p < 0.05$) between the prooxidant effects of compounds **1**, **2e**, and **4b** and their ability to induce apoptosis in their sensitive cancer cells are illustrated in Figure 10. This confirms that their powerful apoptosis-dependent anticancer action is mediated by a prooxidant effect that drives unregulated generation of free radicals in cancer cells, causing DNA damage, which together with the induction of p53 activity and inhibition of its ubiquitination increases and reduces Bax and Bcl-2 expression, respectively, culminating in apoptotic cell death.

2.2.11. In Vivo Validation of the Antitumor Effect of Compound 1. To further support the safety and efficacy results obtained from *in vitro* experiments on cell lines, we conducted an *in vivo* assessment of the antitumor activity and safety of compound **1**, the most active derivative in the series. Similar to our previous work, an MCF-7 xenograft model was established in immunocompromised BALB/c mice.[28] Two million MCF-7 cells in 200 μL of DMEM were injected subcutaneously in the interscapular region to trigger tumor formation. Tumor bearing mice were divided into four groups of five mice, with an *a priori* target of analyzing changes in tumor size in three mice per group, accounting for a 25% loss as the maximal tolerable margin of mortality in each group as per the requirements of our animal ethics protocol for treatment with xenobiotics. Mice in different groups received either 100 μL of DMSO (control group), 5-FU (30 mg/kg in 100 μL of DMSO), NF (50 mg/kg in 100 μL of DMSO), or compound **1** (50 mg/kg in 100 μL of DMSO) by daily intraperitoneal injection for 3 weeks. All of the doses used were presumed to be safe based on the previous literature. 5-FU was used at a dose within the range of its antitumor effect in mice (20−40 mg/kg)[47] but below the threshold reported for tissue injury (50 mg/kg).[48] The dose of NF selected was sufficient to induce detectable DNA damage when used *in vivo* in mice[49] but well below the dose ranges reported for repeated *in vivo* administration (100 mg/kg).[50] The dose selected for compound **1** was 20-fold less than the estimated LD_{50} based on the chemical structure.[51] Nonetheless, the relative impact on mortality was assessed compared to the control group, and survival curves were constructed. As shown in Figure 11A, both 5-FU and compound **1** had a minor effect on mouse survival that was not significantly different from the control. On the other hand, NF at the dose used proved to be significantly more lethal than the control, and hence the experiment for this group was terminated early before the completion of the planned treatment duration.

Three days after the completion of the planned treatment duration of 3 weeks, mice were sacrificed, and the tumor site was exposed. Figure 11B shows that both 5-FU and compound **1**

https://doi.org/10.1021/acs.jmedchem.2c01408
J. Med. Chem. 2023, 66, 4565−4587

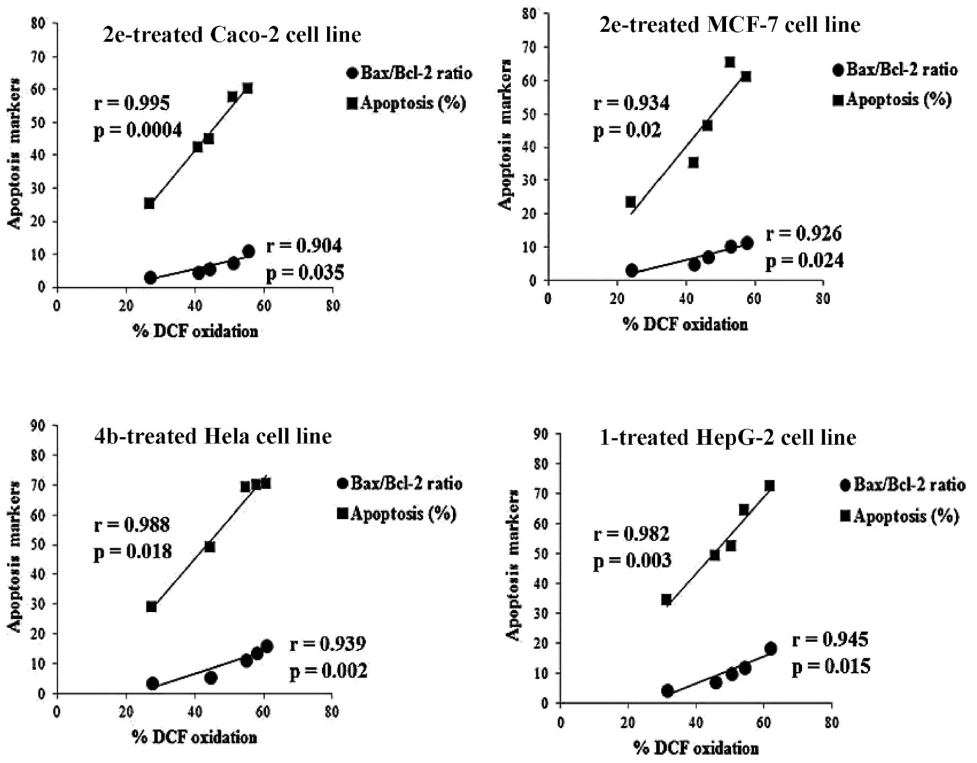

Figure 10. Correlation between the prooxidant effect and apoptosis-mediated anticancer activity of compounds **1**, **2e**, and **4b**.

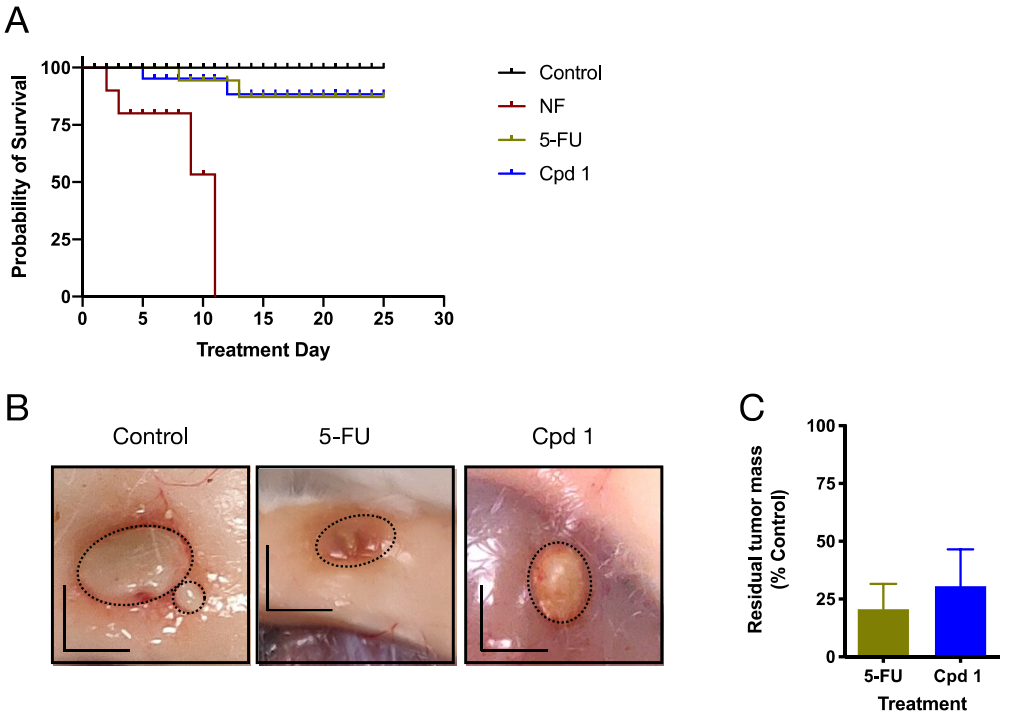

Figure 11. *In vivo* safety and efficacy of compound **1** relative to 5-FU and NF. (A) Survival analysis of mice in different treatment groups (n = 5 at the beginning of treatment) with NF producing a statistically significant increase in mortality as assessed by the log-rank test; (B) representative photographs of tumor size (dotted line contour) in control, 5-FU treated, and compound **1**-treated mouse groups. Scale bars are 5 mm; (C) average tumor mass in 5-FU treated and compound **1**-treated mice as a percentage of control mouse tumor mass (n = 3).

treatment led to tumor size reduction. Indeed, when the tumor masses were excised and weighed, either treatment decreased the tumor mass by ~65−75% (Figure 11C). Taken together, our results indicate that compound **1** is at least equally safe and effective as an antitumor treatment to 5-FU *in vivo*. Further experimentation would be required to determine the optimal dosing strategy and determine the full side effect profile *in vivo*.

2.3. Molecular Docking. *2.3.1. Docking into MDM2 Active Site.* The p53−MDM2 complex is an example of protein/protein interaction. Trp23, Leu26, and Phe19 residues of p53

https://doi.org/10.1021/acs.jmedchem.2c01408
J. Med. Chem. 2023, 66, 4565−4587

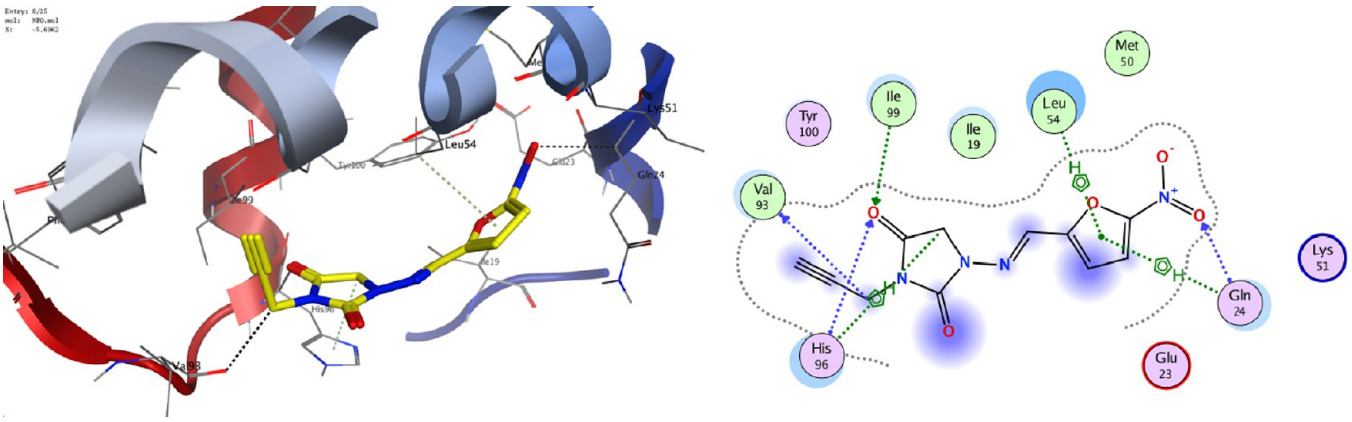

Figure 12. Docking and binding pattern of compound **1** into the MDM2 active site (PDB 3LBL) in 3D (left) and 2D (right) views.

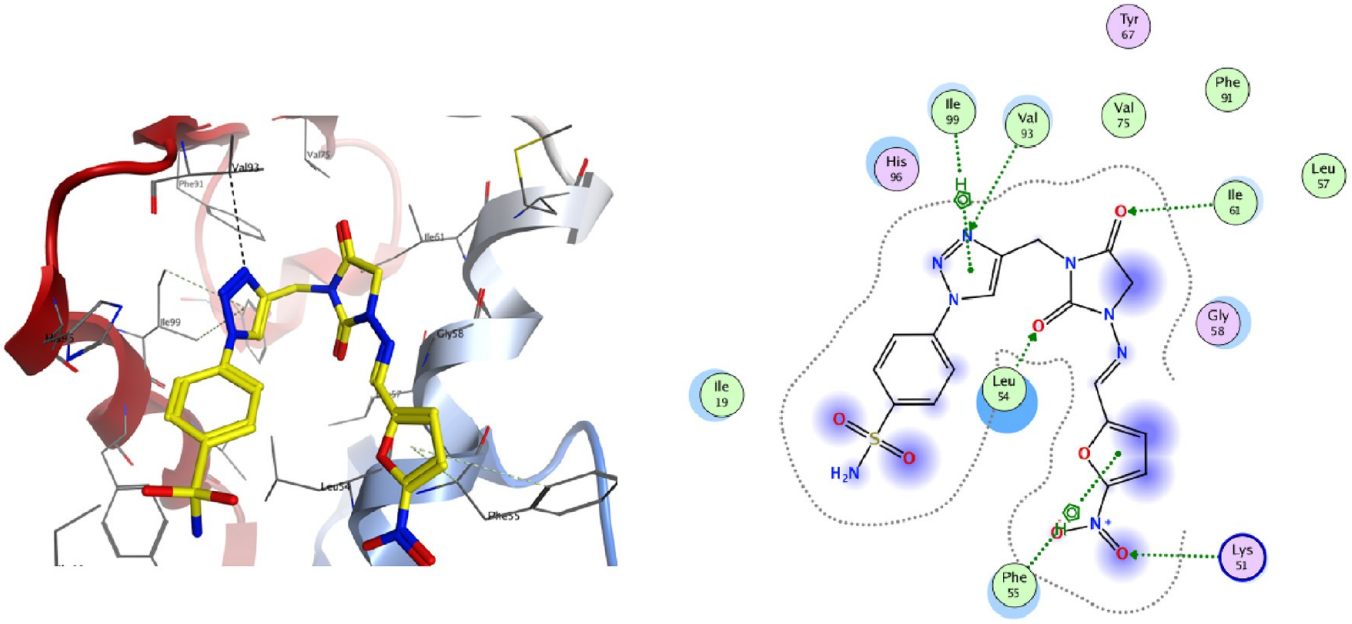

Figure 13. Docking and binding pattern of compound **2e** into the MDM2 active site (PDB 3LBL) in 3D (left) and 2D (right) views.

constitute a "hot spot triad" in the p53−MDM2 complex. These three hydrophobic residues fit into three corresponding hydrophobic pockets, where Trp23's indole nitrogen establishes a hydrogen bond with MDM2's Leu54.[52]

The four crucial p53 amino acids Phe19, Leu22, Trp23, and Leu26 as well as MDM2 residues Leu54, Leu57, Gly58, Ile61, Met62, Tyr67, Gln72, His73, Val75, Phe91, Val93, His96, Ile99, and Tyr100, at the very least, exert the primary roles in this protein/protein interaction.[53]

A docking analysis was conducted to identify the putative molecular interactions participating in the recognition of MDM2 by the most active compounds **1**, **2e**, and **4b**. This was accomplished using Molecular operating environment software (MOE 2019.0102). Protein data bank provided the X-ray crystal structure of human MDM2 protein (PDB ID: 3LBL) with its co-crystallized ligand MI6. (https://www.rcsb.org/structure/3lbl).

The MOE search algorithm and scoring function were used to help identify the optimal binding docking postures. Furthermore, binding energy scores, binding interactions with proximal amino acid residues, and docked compounds' orientation relative to the co-crystalized ligand were all employed to estimate the docked compounds' binding affinities toward the active site. The co-crystallized ligand was also re-docked to verify the selected docking protocol. The original PDB pose was recovered with a root mean square deviation (RMSD) of 0.2 and docking score of −7.3 kcal/mol.

Examination of the binding profile of compound **1** into the MDM2 active site revealed a number of hydrogen bonding interactions, two of which were formed between the carbonyl oxygen of the hydantoin moiety at position 4, as an acceptor, and the key amino acids His96 and Ile99. More hydrogen bonds were displayed between one of the nitro group oxygens, as an acceptor, and Gln24. This is in addition to a hydrogen bond between CH_2 of the propargyl group and Val93. Furthermore, two arene-hydrogen contacts were displayed between the furan ring and Gln24 as well as Leu54. Also, His96 formed an arene-hydrogen interaction with C5-H of the hydantoin moiety (−5.7 kcal/mol) (Figure 12).

Investigation of the best-docked pose of the 1,2,3-triazole derivative **2e** showed that it was smoothly anchored in the active site of MDM2 with a binding energy score of −6.8 kcal/mol (Figure 13). It was held in the binding pocket through hydrogen bonding between one of the nitro group oxygens and Lys51.

https://doi.org/10.1021/acs.jmedchem.2c01408
J. Med. Chem. 2023, 66, 4565−4587

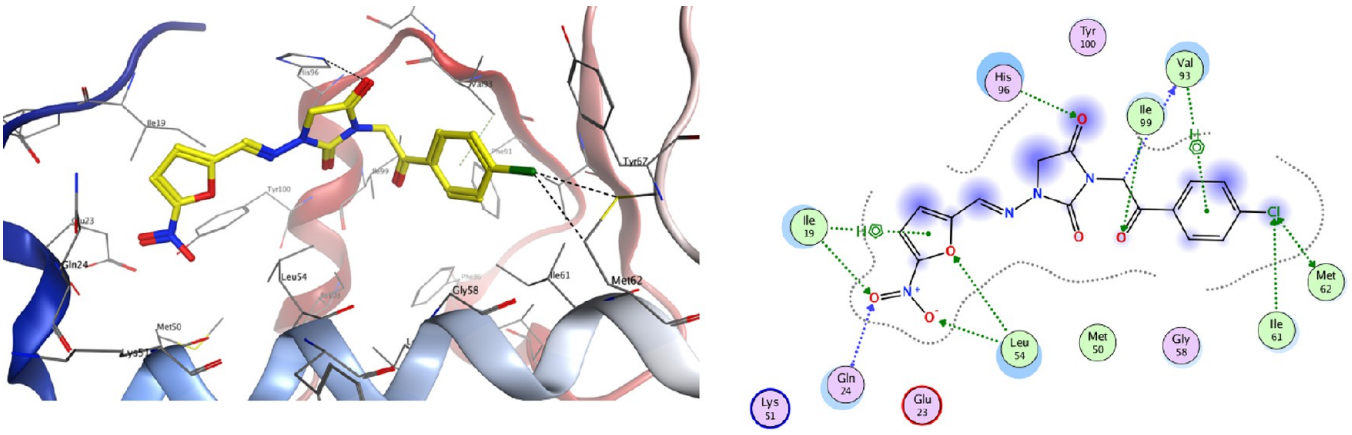

Figure 14. Docking and binding pattern of compound **4b** into the MDM2 active site (PDB 3LBL) in 3D (left) and 2D (right) views.

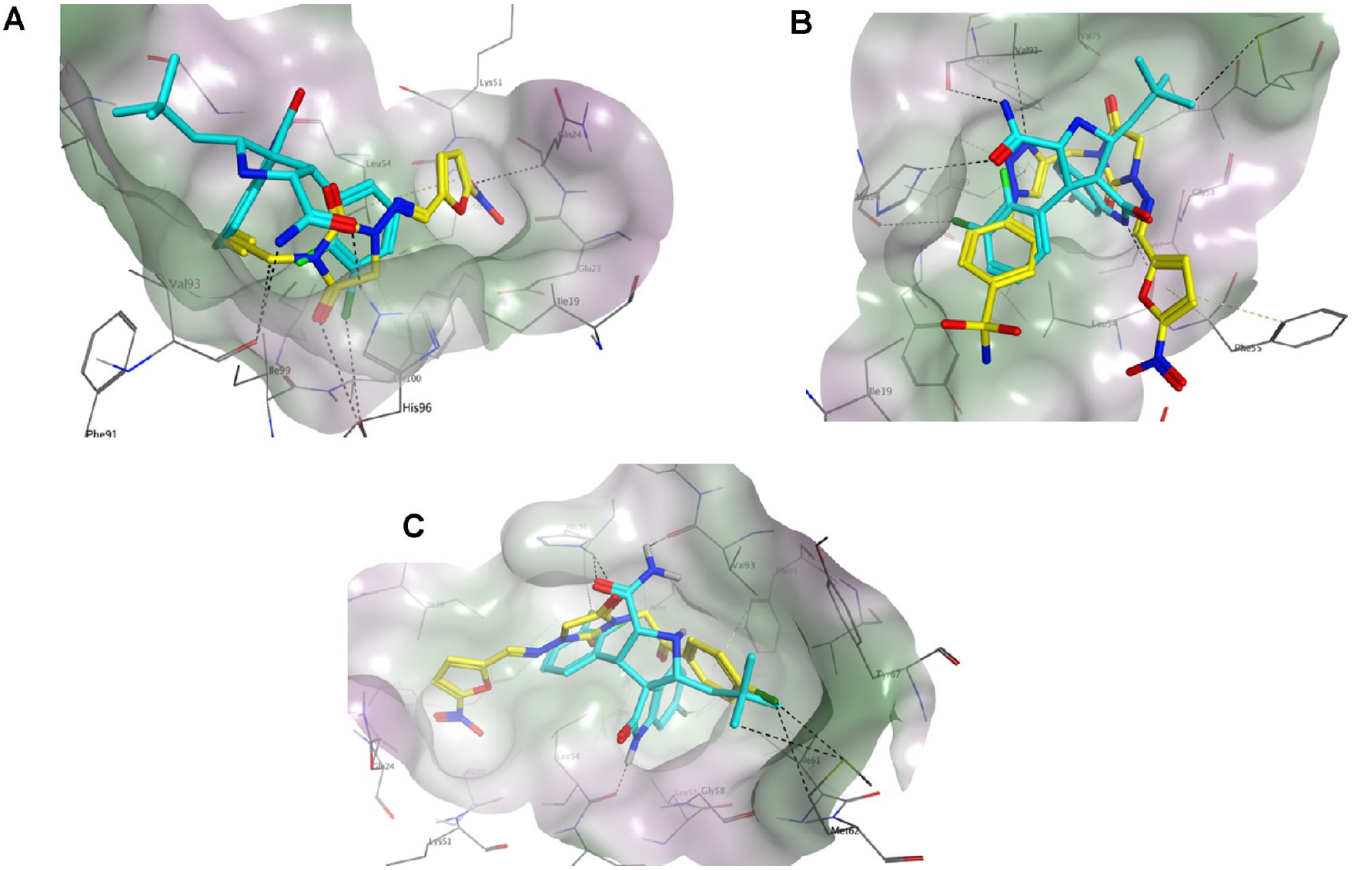

Figure 15. Overlay of the docked poses of compounds **1** (A), **2e** (B), and **4b** (C) (in yellow) with the co-crystallized ligand **MI6** (in cyan) into the MDM2 active site (PDB 3LBL). Lipophilic and hydrophilic regions of the active site were displayed as green and red colored molecular surfaces, respectively.

Both carbonyl oxygens of the hydantoin moiety established two hydrogen bonds with the crucial amino acid residues Leu54 and Ile61. Interestingly, the 1,2,3-triazole ring participated in further stabilization of the formed complex via hydrogen bond interaction of its N3 with Val93 and arene-hydrogen contact with Ile99, hence highlighting its pharmacophoric significance. As well, another arene−hydrogen interaction was observed between the furan ring and Phe55.

As shown in Figure 14, compound **4b** was perfectly lodged in the active site by forming several hydrogen bond interactions such as those demonstrated between Ile19, Gln24, and Leu54 residues and the nitro furan moiety. Additionally, the *p*-chloro phenacyl moiety established around four hydrogen bonds with Ile61, Met62, Val93, and Ile99. As well, both moieties were engaged in arene hydrogen contacts with Ile19 and Val93 and thus reinforcing the predicted binding affinity (−6.6 kcal/mol).

It is also worth mentioning that an overlay of each of the docking poses of the three compounds over the co-crystallized ligand MI6 (Figure 15) showed that they occupied the same spatial area and position as observed with MI6. The latter was reported to perfectly accommodate the three hydrophobic pockets of the hot spot triad.[52,54]

https://doi.org/10.1021/acs.jmedchem.2c01408
J. Med. Chem. 2023, 66, 4565−4587

3. CONCLUSIONS

A synthetic biology-oriented drug repurposing approach was adopted exploiting the antibacterial drug nitrofurantoin in the field of cancer. Hence, 15 derivatives were properly designed and synthesized via N-alkylation and copper-catalyzed azide-alkyne click reaction. Most of the compounds displayed submicromolar IC_{50} values in cytotoxicity evaluation in four cancer cell lines Caco-2, MCF-7, HeLa, and HepG-2 cells. They were safe when tested in the non-cancerous Wi-38 cell line with selectivity indices of more than 3 for the most active derivatives. Significant cytotoxic activity was reflected as severe morphological changes in the tested cancer cells. Mechanistic studies revealed that the most active compounds **1**, **2e**, and **4b** triggered apoptosis by evoking a severe oxidative redox state leading to apoptotic cell death involving downregulation of Bcl2 and upregulation of Bax followed by caspase 3/7 activation. Indeed, positive linear correlation was shown between the oxidative load produced in the cells and the subsequent increase in apoptotic markers.

Significantly, time- and concentration-dependent DNA damage proved to contribute to the anticancer activity of compound **1**, which was demonstrated by pATM nuclear shuttling. Also, the cell death brought about by the latter was p53-dependent. The three most active compounds inhibited p53−MDM2 interaction with submicromolar IC_{50} values. This was effectively substantiated via molecular docking of the most active compounds into the active site of MDM2, showing high affinity and adopting favorable binding modes. Interestingly, the sensitivity of UC3 cells to the cytotoxic effects of ionizing radiation was markedly enhanced using low non cytotoxic concentrations of compound **1** possibly being a function of increased p53 expression. The MCF-7 xenograft model experiment confirmed the *in vivo* antitumor activity and safety of the most active derivative in the series. These findings provide concrete evidence for the convenience of these repurposed nitrofurantoin derivatives for the development of promising anticancer agents as well as low dose combination therapy with radiation.

4. EXPERIMENTAL SECTION

4.1. Chemistry. All chemicals were purchased from commercial suppliers and used without further purification. Nitrofurantoin was generously supplied by the Alexandria Scientific office of Medical Union Pharmaceuticals (MUP). Melting points were recorded on electrotherm capillary tube Stuart melting point apparatus SMP10 and are all uncorrected. Follow up of the reactions' rates were performed by thin-layer chromatography (TLC) on silica gel-precoated aluminum sheets (Type 60 GF254; Merck; Germany), and the spots were visualized by exposure to iodine vapors or UV-lamp at λ of 254 nm for a few seconds. Infrared spectra (IR) were recorded using KBr discs on a Shimadzu IR 435 spectrophotometer, Faculty of Pharmacy, Cairo University. Nuclear magnetic resonance (^{1}H NMR and ^{13}C NMR) spectra were recorded on a Jeol JNM ECA 500II spectrometer (500 MHz, 11.75 Tesla) at the NMR Unit, Faculty of Science, Mansoura University or on a Bruker (400 MHz) spectrometer, Faculty of Pharmacy, Cairo University using deuterated dimethylsulfoxide (DMSO-d_6) as solvent. The data were recorded as chemical shifts expressed in δ (ppm) relative to tetramethylsilane (TMS) as internal standard. Signal splitting are expressed by the following abbreviations: s = singlet, d = doublet, t = triplet, q = quartet and m = multiplet. The purity of the new compounds was checked by elemental analyses (C, H, N, and S), conducted on a FLASH 2000 CHNS/O analyzer, Thermo Scientific at the regional center for mycology and biotechnology (RCMB), Al-Azhar University. In addition, new compounds were found to be ≥95% pure by reversed phase HPLC analysis using an HC-C-18 reverse phase HPLC column (Agilent technologies, USA, 150 mmx4.6 mm I.D; particle size 5 μm) equipped with G1211C pump and G1315D photodiode array detector. The output of the signal was monitored and integrated using Agilent chemstation software.

An injection volume of 20 μL, flow rate of 1 mL/min, and mobile phase consisting of phosphate-buffered saline (PBS) pH 7.4, methanol, and acetonitrile in the ratio of 4:4:2 v/v, respectively, were applied. Analyses were monitored at 254 nm wavelength.

*4.1.1. General Procedure for Synthesis of Alkylated Products **1**, **3a−c**, and **4a−e**.* A mixture of nitrofurantoin (0.238 g, 1 mmol) and potassium carbonate (0.41 g, 3 mmol) in DMF was stirred at room temperature for 1 h. Propargyl bromide (for compound **1**), the appropriate benzyl halide (for compounds **3a−c**), or the appropriate phenacyl bromide (for compounds **4a−e**) (1 mmol) was added and stirring was continued at room temperature for 48 h. The mixture was then poured on ice, filtered, washed with water, dried, and recrystallized from ethanol/DMF.

*4.1.1.1. (E)-1-(((5-Nitrofuran-2-yl)methylene)amino)-3-(prop-2-yn-1-yl)imidazolidine-2,4-dione (**1**).* Orange-brown powder. Yield 93%. m.p. 208−210 °C. IR (KBr, cm^{-1}): 3245.38 (C≡C−H), 2200.23 (C≡C), 1786.35 (C=O), 1734.43 (C=O), 1630.33 (C=N), 1561.353 (C=C), 1250.58 (C−O−C). ^{1}H NMR (400 MHz, DMSO-d_6): δ (ppm) 3.18 (s, 1H, ≡C-H), 4.29 (s, 2H, $\underline{CH_2}$-C≡C-H), 4.50 (s, 2H, imidazolidinedione-C_5-H), 7.20 (s, 1H, furan-C_3-H), 7.80 (s, 1H, furan-C_4-H), 7.90 (s, 1H, C$\underline{H}$=N). ^{13}C NMR (100 MHz, DMSO-d_6): δ (ppm) 28.2, 48.9, 74.7, 78.1, 115.1, 115.5132.7, 151.9, 152.2, 152.3, 166.9. Anal. calcd (%) for $C_{11}H_8N_4O_5$ (276.21): C, 47.83; H, 2.92; N, 20.28. Found C, 48.10; H, 3.08; N, 20.61. HPLC/DAD: Retention time 2.54 min.

*4.1.2. General Procedure for Synthesis of the Triazoles **2a−f**.* To a mixture of (*E*)-1-(((5-nitrofuran-2-yl)methylene)amino)-3-(prop-2-yn-1-yl)imidazolidine-2,4-dione (**1**) (0.276 g, 1 mmol) and the appropriate aryl azide (1.5 mmol) in 10 mL of DMF were added an aqueous solution (5 mL) of sodium ascorbate (0.06 g, 0.34 mmol) and $CuSO_4{\cdot}5H_2O$ (0.02 g, 0.085 mmol). The mixture was stirred at room temperature for 48 h, then poured on ice, filtered, washed with cold water, dried, and recrystallized from ethanol/DMF.

*4.1.2.1. (E)-1-(((5-Nitrofuran-2-yl)methylene)amino)-3-((1-phenyl-1H-1,2,3-triazol-4-yl)methyl)imidazolidine-2,4-dione (**2a**).* Dark brown powder. Yield 83%. m.p. 218 °C. IR (KBr, cm^{-1}): 1783.02 (C=O), 1726.38 (C=O), 1503.66 (C=C), 1249.24 (C−O−C). ^{1}H NMR (400 MHz, DMSO-d_6): δ (ppm) 4.51 (s, 2H, imidazolidinedione-C_5-H), 4.85 (s, 2H, -CH_2-), 7.19 (s, 1H, furan-C_3-H), 7.20−7.79 (m, 6H, furan-C_4-H and phenyl-$C_{2,3,4,5,6}$-H), 7.88 (s, 1H, C$\underline{H}$=N), 8.78 (s, 1H, triazole-C_5-H). ^{13}C NMR (100 MHz, DMSO-d_6): δ (ppm) 34.3, 48.9, 115.1, 115.3, 120.5, 122.2, 129.2, 130.4, 132.5, 136.9, 152.1, 152.3, 152.8, 167.4. Anal. calcd (%) for $C_{17}H_{13}N_7O_5$ (395.34): C, 51.65; H, 3.31; N, 24.80. Found C, 51.90; H, 3.42; N, 24.63. HPLC/DAD: Retention time 16.42 min.

*4.1.2.2. (E)-3-((1-(4-Chlorophenyl)-1H-1,2,3-triazol-4-yl)methyl)-1-(((5-nitrofuran-2-yl)methylene)amino)imidazolidine-2,4-dione (**2b**).* Beige powder. Yield 87%. m.p. 188−190 °C. IR (KBr, cm^{-1}): 1782.01 (C=O), 1725.31 (C=O), 1501.41 (C=C), 1250.66 (C−O−C). ^{1}H NMR (400 MHz, DMSO-d_6): δ (ppm) 4.51 (s, 2H, imidazolidinedione-C_5-H), 4.85 (s, 2H, -CH_2-), 7.19 (s, 1H, furan-C_3-H), 7.20−7.79 (m, 5H, furan-C_4-H and phenyl-$C_{2,3,5,6}$-H), 7.88 (s, 1H, C$\underline{H}$=N), 8.78 (s, 1H, triazole-C_5-H). ^{13}C NMR (100 MHz, DMSO-d_6): δ (ppm) 34.3, 48.9, 115.1, 115.3120.5, 122.2, 129.2, 130.4, 132.5, 136.9, 152.1, 152.3, 152.8, 167.4. Anal. calcd (%) for $C_{17}H_{12}ClN_7O_5$ (429.78): C, 47.51; H, 2.81; N, 22.81. Found C, 47.76; H, 2.97; N, 23.12. HPLC/DAD: Retention time 4.65 min.

*4.1.2.3. (E)-1-(((5-Nitrofuran-2-yl)methylene)amino)-3-((1-(4-nitrophenyl)-1H-1,2,3-triazol-4-yl)methyl)imidazolidine-2,4-dione (**2c**).* Brown powder. Yield 86%. m.p. 168−170 °C. IR (KBr, cm^{-1}): 1780.30 (C=O), 1722.25 (C=O), 1525.86 (C=C), 1246.06 (C−O−C). ^{1}H NMR (500 MHz, DMSO-d_6): δ (ppm) 4.46 (s, 2H, imidazolidinedione-C_5-H), 4.82 (s, 2H, -CH_2-), 7.14 (s, 1H, furan-C_3-H), 7.75 (s, 1H, furan-C_4-H), 7.87 (s, 1H, C$\underline{H}$=N), 8.16 (d, J = 10 Hz, 2H, phenyl-$C_{2,6}$-H), 8.40 (d, J = 10 Hz, 2H, phenyl-$C_{3,5}$-H), 8.96 (s, 1H, triazole-C_5-H). ^{13}C NMR (125 MHz, DMSO-d_6): δ (ppm) 34.3, 49, 112.9, 115.2, 115.4, 121.1, 122.7, 126.1, 126.9, 132.6, 141.2, 144.2,

https://doi.org/10.1021/acs.jmedchem.2c01408
J. Med. Chem. 2023, 66, 4565−4587

147.3, 152.1, 152.4, 152.9, 167.4. Anal. calcd (%) for $C_{17}H_{12}N_8O_7$ (440.33): C, 46.64; H, 3.02; N, 25.71. Found C, 46.37; H, 2.75; N, 25.45. HPLC/DAD: Retention time 2.61 min.

*4.1.2.4. (E)-1-(((5-Nitrofuran-2-yl)methylene)amino)-3-((1-(p-tolyl)-1H-1,2,3-triazol-4-yl)methyl)imidazolidine-2,4-dione (**2d**).* Brown powder. Yield 90%. m.p. 240−242 °C. IR (KBr, cm^{-1}): 1783.26 (C═O), 1728.04 (C═O), 1521.07 (C═C), 1251.95 (C−O−C). ^{1}H NMR (500 MHz, DMSO-d_6): δ (ppm) 2.32 (s, 3H, -CH_3), 4.45 (s, 2H, imidazolidinedione-C_5-H), 4.77 (s, 2H, -CH_2-), 7.13 (s, 1H, furan-C_3-H), 7.34 (d, J = 10 Hz, 2H, phenyl-$C_{3,5}$-H), 7.70 (d, J = 10 Hz, 2H, phenyl-$C_{2,6}$-H), 7.75 (s, 1H, furan-C_4-H), 7.86 (s, 1H, C<u>H</u>═N), 8.66 (s, 1H, triazole-C_5-H). ^{13}C NMR (125 MHz, DMSO-d_6): δ (ppm) 21.1, 34.4, 49, 115.2, 115.4, 120.4, 122.1, 130.8, 132.5, 134.8, 138.9, 143.4, 152.1, 152.4, 152.9, 167.5. Anal. calcd (%) for $C_{18}H_{15}N_7O_5$ (409.11): C, 52.81; H, 3.69; N, 23.95. Found C, 52.96; H, 3.87; N, 24.12. HPLC/DAD: Retention time 3.74 min.

*4.1.2.5. (E)-4-(4-((3-(((5-Nitrofuran-2-yl)methylene)amino)-2,5-dioxoimidazolidin-1-yl)methyl)-1H-1,2,3-triazol-1-yl)-benzenesulfonamide (**2e**).* Dark brown powder. Yield 80%. m.p. >350 °C. IR (KBr, cm^{-1}): 3167.23 (NH), 1783.36 (C═O), 1727.54 (C═O), 1529.76 (C═C), 1347.26 (SO_2), 1249.40 (C−O−C). ^{1}H NMR (500 MHz, DMSO-d_6): δ (ppm) 4.45 (s, 2H, imidazolidinedione-C_5-H), 4.79 (s, 2H, -CH_2-), 6.80 (br. s, 2H, SO_2NH_2), 7.13 (s, 1H, furan-C_3-H), 7.74 (s, 1H, furan-C_4-H), 7.86 (s, 1H, C<u>H</u>═N), 7.94−8.00 (m, 4H, phenyl-$C_{2,3,5,6}$-H), 8.80 (s, 1H, triazole-C_5-H). ^{13}C NMR (125 MHz, DMSO-d_6): δ (ppm) 34.3, 49, 115.2, 115.5, 120.9, 122.5, 128.2, 132.6, 139.1, 142.7, 143.9, 152.1, 152.4, 152.9, 167.4. Anal. calcd (%) for $C_{18}H_{15}N_7O_5S$ (474.41): C, 43.04; H, 2.97; N, 23.62; S, 6.76. Found C, 42.89; H, 3.09; N, 23.90; S, 6.88. HPLC/DAD: Retention time 4.15 min.

*4.1.2.6. (E)-4-(4-((3-(((5-Nitrofuran-2-yl)methylene)amino)-2,5-dioxoimidazolidin-1-yl)methyl)-1H-1,2,3-triazol-1-yl)-N-(thiazol-2-yl)benzenesulfonamide (**2f**).* Light brown powder. Yield 83%. m.p. 167−169 °C. IR (KBr, cm^{-1}): 3167.23 (NH), 1785.40 (C═O), 1723.76 (C═O), 1627.55 (C═N), 1591.41 (C═C), 1347.26 (SO_2), 1250.48, 1018.97 (C−O−C). ^{1}H NMR (400 MHz, DMSO-d_6): δ (ppm) 4.53 (s, 2H, imidazolidinedione-C_5-H), 4.88 (s, 2H, -CH_2-), 7.19 (s, 1H, furan-C_3-H), 7.54−8.12 (m, 7H, furan-C_4-H, thiazolyl-$C_{4,5}$-H and phenyl-$C_{2,3,5,6}$-H), 8.04 (s, 1H, C<u>H</u>═N), 8.90 (s, 1H, triazole-C_5-H). ^{13}C NMR (100 MHz, DMSO-d_6): δ (ppm) 34.3, 48.9, 115.1, 115.4, 120.0, 120.7, 122.4, 128.0, 132.5, 138.9, 143.8, 144.4, 152.0, 152.3, 152.8, 162.8, 167.4. Anal. calcd (%) for $C_{20}H_{15}N_9O_7S_2$ (557.52): C, 43.09; H, 2.71; N, 22.61; S, 11.50. Found C, 43.34; H, 2.75; N, 22.86; S, 11.42. HPLC/DAD: Retention time 2.84 min.

*4.1.2.7. (E)-3-Benzyl-1-(((5-nitrofuran-2-yl)methylene)amino)-imidazolidine-2,4-dione (**3a**).*[55] Reddish-brown powder. Yield 68%. m.p. 188−190 °C. IR (KBr, cm^{-1}): 1782.34 (C═O), 1724.72 (C═O), 1629.99 (C═N), 1588.21 (C═C), 1250.48, 1018.97 (C−O−C). ^{1}H NMR (400 MHz, DMSO-d_6): δ (ppm) 4.52 (s, 2H, imidazolidine-dione-C_5-H), 4.71 (s, 2H, C<u>H</u>$_2$-benzyl), 7.18 (d, 1H, J = 3.92 Hz, furan-C_3-H), 7.31−7.36 (m, 5H, benzyl-$C_{2,3,4,5,6}$-H), 7.78 (d, 1H, J = 3.92 Hz, furan-C_4-H), 7.91 (s, 1H, C<u>H</u>═N). ^{13}C NMR (100 MHz, DMSO-d_6): δ (ppm) 42.2, 48.9, 115.1, 115.3, 128.4, 128.9, 133.6, 136.0, 152.1, 152.3, 153.2, 167.8. Anal. calcd (%) for $C_{15}H_{12}N_4O_5$ (328.28): C, 54.88; H, 3.68; N, 17.07. Found C, 55.15; H, 3.84; N, 17.33. HPLC/DAD: Retention time 2.61 min.

*4.1.2.8. (E)-3-(4-Bromobenzyl)-1-(((5-nitrofuran-2-yl)methylene)-amino)imidazolidine-2,4-dione (**3b**).*[55] Yellow powder. Yield 88%. m.p. >350 °C. IR (KBr, cm^{-1}): 1783.79 (C═O), 1724.71 (C═O), 1625.06 (C═N), 1585.41 (C═C), 1249.90, 1071.83 (C−O−C). ^{1}H NMR (500 MHz, DMSO-d_6): δ (ppm) 4.44 (s, 2H, imidazolidine-dione-C_5-H), 4.60 (s, 2H, C<u>H</u>$_2$−4-bromobenzyl), 7.13 (d, 1H, J = 5 Hz, furan-C_3-H), 7.26 (d, 2H, J = 5 Hz, 4-bromobenzyl-$C_{2,6}$-H), 7.50 (d, 2H, J = 5 Hz, 4-bromobenzyl-$C_{3,5}$-H), 7.74 (d, 1H, J = 5 Hz, furan-C_4-H), 7.84 (s, 1H, C<u>H</u>═N). ^{13}C NMR (125 MHz, DMSO-d_6): δ (ppm) 41.7, 49, 115.2, 115.4, 121.3, 130.4, 131.9, 132.4, 135.9, 152.2, 152.4, 153.2, 167.8. Anal. calcd (%) for $C_{15}H_{11}BrN_4O_5$ (407.18): C, 44.25; H, 2.72; N, 13.76. Found C, 44.08; H, 2.91; N, 14.02. HPLC/DAD: Retention time 4 min.

*4.1.2.9. (E)-3-(4-Nitrobenzyl)-1-(((5-nitrofuran-2-yl)methylene)-amino)imidazolidine-2,4-dione (**3c**).*[55] Yellow powder. Yield 74%. m.p. 166−168 °C. IR (KBr, cm^{-1}): 1786.54 (C═O), 1727.56 (C═O), 1632.09 (C═N), 1606.39 (C═C), 1250.58, 1019.66 (C−O−C). ^{1}H NMR (500 MHz, DMSO-d_6): δ (ppm) 4.47 (s, 2H, imidazolidine-dione-C_5-H), 4.78 (s, 2H, C<u>H</u>$_2$−4-nitrobenzyl), 7.14 (s, 1H, furan-C_3-H), 7.59 (d, J = 8 Hz, 2H, 4-nitrobenzyl-$C_{2,6}$-H), 7.75 (s, 1H, furan-C_4-H), 7.87 (s, 1H, C<u>H</u>═N), 8.16 (d, J = 8 Hz, 2H, 4-nitrobenzyl-$C_{3,5}$-H). ^{13}C NMR (125 MHz, DMSO-d_6): δ (ppm) 41.7, 49.1, 115.2, 115.5, 124.1, 129.3, 132.6, 144.1, 144.3, 147.5, 152.1, 152.4, 153.2, 167.9. Anal. calcd (%) for $C_{15}H_{11}N_5O_7$ (373.28): C, 48.27; H, 2.97; N, 18.76. Found C, 48.54; H, 3.05; N, 18.93. HPLC/DAD: Retention time 2.9 min.

*4.1.2.10. (E)-1-(((5-Nitrofuran-2-yl)methylene)amino)-3-(2-oxo-2-phenylethyl)imidazolidine-2,4-dione (**4a**).* Dark orange powder. Yield 69%. m.p. >350 °C. IR (KBr, cm^{-1}): 1782.15 (C═O), 1727.60 (C═O), 1631.22 (C═N), 1581.63 (C═C), 1229.91 (C-O-C). ^{1}H NMR (500 MHz, DMSO-d_6): δ (ppm) 4.63 (s, 2H, imidazolidine-dione-C_5-H), 5.11 (s, 2H, COC<u>H</u>$_2$-phenacyl), 7.17 (d, J = 5 Hz, 1H, furan-C_3-H), 7.68−7.71 (m, 3H, phenacyl-$C_{3,4,5}$-H), 7.76 (d, J = 5 Hz, 1H, furan-C_4-H), 7.89 (s, 1H, C<u>H</u>═N), 8.04 (d, J = 8 Hz, 2H, phenacyl-$C_{2,6}$-H). ^{13}C NMR (125 MHz, DMSO-d_6): δ (ppm) 45.6, 48.9, 115.2, 115.6, 128.8, 129.6, 133, 134.4, 134.9, 152, 152.4, 152.9, 167.7, 192.3. Anal. calcd (%) for $C_{16}H_{12}N_4O_6$ (356.29): C, 53.94; H, 3.39; N, 15.73. Found C, 54.12; H, 3.60; N, 16.04. HPLC/DAD: Retention time 17.13 min.

*4.1.2.11. (E)-3-(2-(4-Chlorophenyl)-2-oxoethyl)-1-(((5-nitrofuran-2-yl)methylene)amino) imidazolidine-2,4-dione (**4b**).* Dark brown powder. Yield 81%. m.p. 182−184 °C. IR (KBr, cm^{-1}): 1789.74 (C═O), 1728.01 (C═O), 1628.52 (C═N), 1589.83 (C═C), 1229.77, 1091.55 (C-O-C). ^{1}H NMR (400 MHz, DMSO-d_6): δ (ppm) 4.68 (s, 2H, imidazolidinedione-C_5-H), 5.17 (s, 2H, COC<u>H</u>$_2$−4-chlorophenacyl), 7.22 (d, 1H, J = 3.84 Hz, furan-C_3-H), 7.67 (d, 2H, J = 8.44 Hz, 4-chloro phenacyl-$C_{3,5}$-H), 7.80 (d, 1H, J = 3.84 Hz, furan-C_4-H), 7.94 (s, 1H, C<u>H</u>═N), 8.11 (d, 2H, J = 8.44 Hz, 4-chloro phenacyl-$C_{2,6}$-H). ^{13}C NMR (100 MHz, DMSO-d_6): δ (ppm) 45.5, 48.8, 115.1, 115.6, 129.6, 130.7, 132.9, 133.0, 139.8, 151.9, 152.3, 152.8, 167.6, 191.5. Anal. calcd (%) for $C_{16}H_{11}ClN_4O_6$ (390.74): C, 49.18; H, 2.84; N, 14.34. Found C, 48.86; H, 3.07; N, 14.70. HPLC/DAD: Retention time 3.6 min.

*4.1.2.12. (E)-3-(2-(4-Bromophenyl)-2-oxoethyl)-1-(((5-nitrofuran-2-yl)methylene)amino)imidazolidine-2,4-dione (**4c**).* Light brown powder. Yield 76%. m.p. 209−211 °C. IR (KBr, cm^{-1}): 1786.61 (C═O), 1722.96 (C═O), 1630.11 (C═N), 1585.01 (C═C), 1251.68, 1071.96 (C−O−C). ^{1}H NMR (400 MHz, DMSO-d_6): δ (ppm) 4.68 (s, 2H, imidazolidinedione-C_5-H), 5.16 (s, 2H, COC<u>H</u>$_2$−4-bromophenacyl), 7.22 (d, 1H, J = 4 Hz, furan-C_3-H), 7.80 (s, 1H, furan-C_4-H), 7.81 (d, 2H, J = 8 Hz, 4-bromophenacyl-$C_{3,5}$-H), 7.94 (s, 1H, C<u>H</u>═N), 8.02 (d, 2H, J = 8 Hz, 4-bromophenacyl-$C_{2,6}$-H). ^{13}C NMR (100 MHz, DMSO-d_6): δ (ppm) 45.5, 48.9, 115.1, 115.6, 129.1, 130.7, 132.2, 132.6, 132.9, 133.3, 152, 152.4, 152.8, 167.6, 191.7. Anal. calcd (%) for $C_{16}H_{11}BrN_4O_6$ (435.19): C, 44.16; H, 2.55; N, 12.87. Found C, 44.50; H, 2.79; N, 13.15. HPLC/DAD: Retention time 3.04 min.

*4.1.2.13. (E)-1-(((5-Nitrofuran-2-yl)methylene)amino)-3-(2-oxo-2-(p-tolyl)ethyl)imidazolidine-2,4-dione (**4d**).* Brown powder. Yield 82%. m.p. 199−201 °C. IR (KBr, cm^{-1}): 1789.40 (C═O), 1727.10 (C═O), 1633.58 (C═N), 1606.22 (C═C), 1249.26, 1015.54 (C−O−C). ^{1}H NMR (400 MHz, DMSO-d_6): δ (ppm) 2.42 (s, 3H, CH_3), 4.68 (s, 2H, imidazolidinedione-C_5-H), 5.12 (s, 2H, COC<u>H</u>$_2$−4-methylphenacyl), 7.22 (d, 1H, J = 3.84 Hz, furan-C_3-H), 7.40 (d, 2H, J = 7.88 Hz, 4-methylphenacyl-$C_{2,6}$-H), 7.79 (d, 1H, J = 3.84 Hz, furan-C_4-H), 7.94 (s, 1H, C<u>H</u>═N), 7.99 (d, 2H, J = 7.88 Hz, 4-methylphenacyl-$C_{3,5}$-H). ^{13}C NMR (100 MHz, DMSO-d_6): δ (ppm) 21.7, 45.4, 48.8, 115.1, 115.6, 128.8, 130.0, 131.9, 132.9, 145.5, 151.9, 152.3, 152.9, 167.6, 191.6. Anal. calcd (%) for $C_{17}H_{14}N_4O_6$ (370.32): C, 55.14; H, 3.81; N, 15.13. Found C, 55.54; H, 4.02; N, 15.39. HPLC/DAD: Retention time 4.2 min.

*4.1.2.14. (E)-3-(2-(4-Methoxyphenyl)-2-oxoethyl)-1-(((5-nitrofuran-2-yl)methylene)amino)imidazolidine-2,4-dione (**4e**).* Yellowish-orange powder. Yield 78%. m.p. 149−151 °C. IR (KBr, cm^{-1}): 1783.50 (C═O), 1732.52, 1681.84 (C═O), 1635.27 (C═N), 1599.16 (C═

https://doi.org/10.1021/acs.jmedchem.2c01408
J. Med. Chem. 2023, 66, 4565−4587

C), 1243.65, 1018.91 (C−O−C). ^{1}H NMR (500 MHz, DMSO-d_6): δ (ppm) 3.83 (s, 3H, OCH_3), 4.62 (s, 2H, imidazolidinedione-C_5-H), 5.04 (s, 2H, $COCH_2$−4-methoxyphenacyl), 7.05 (d, 2H, J = 10 Hz, 4-methoxyphenacyl-$C_{3,5}$-H), 7.16 (d, 1H, J = 5 Hz, furan-C_3-H), 7.75 (d, 1H, J = 5 Hz, furan-C_4-H), 7.88 (s, 1H, CH═N), 8.01 (d, 2H, J = 10 Hz, 4-methoxyphenacyl-$C_{2,6}$-H). ^{13}C NMR (125 MHz, DMSO-d_6): δ (ppm) 45.3, 48.9, 56.2, 114.8, 115, 115.2, 115.6, 127.3, 128.4, 131.2, 132.9, 152, 152.4, 153, 164.5, 167.7, 190.4. Anal. calcd (%) for $C_{17}H_{14}N_4O_7$ (386.32): C, 52.85; H, 3.65; N, 14.50. Found C, 52.71; H, 3.89; N, 14.72. HPLC/DAD: Retention time 2.8 min.

4.2. Biological Evaluation. *4.2.1. Determination of Cytotoxicity of Test Compounds to the Normal Human Cell Line.* The normal human lung fibroblast Wi-38 cell line was used to detect cytotoxicity of test compounds compared to the currently used anticancer drug (5-fluorouracil). The Wi-38 cell line was subcultured in DMEM medium-contained 10% fetal bovine serum (FBS), seeded as 5×10^3 cells per well in a 96-well cell culture plate, and incubated at 37 °C in a 5% CO_2 incubator. After 24 h for cell attachment, serial concentrations of test compounds and 5-fluorouracil (5-FU) were incubated with Wi-38 cells for 72 h. Cell viability was assayed by the MTT method.[28,56] 20 μL of 5 mg/mL MTT (Sigma, USA) was added to each well, and the plate was incubated at 37 °C for 3 h. Then, the MTT solution was removed, 100 μL of DMSO was added, and the absorbance of each well was measured with a microplate reader (BMG LabTech, Germany) at 570 nm. The half maximal inhibitory concentration (IC_{50}) and safe dose (EC_{100}) values of the tested compounds that cause 50% and 100% cell viability were estimated by the Graphpad Instat software.

4.2.2. Determination of Anticancer Activity of Test Compounds. The anticancer effect of the abovementioned samples was assayed using five human cancer cell lines. The colon cancer cell line (Caco-2) was maintained in DMEM (Lonza, USA) containing 10% FBS (Gibco, USA) while the breast cancer cell line (MCF-7, MDA-MB-231), cervical cancer cell line (HeLa), and liver cancer cell line (HepG-2) were cultured in RPMI-1640 (Lonza, USA) supplemented with 10% FBS. All cancer cell suspensions (5×10^3 cells/well) were seeded into sterile 96-well plates and allowed to attach for 24 h. Then, serial concentrations of the tested samples and 5-FU were added to four cancer cell lines and plates were incubated for 24 or 72 h at 37 °C in a 5% CO_2 incubator. Viability was assessed by the MTT method, and IC_{50} values were calculated as described above.[28,56] Additionally, the selectivity index (SI) defined as the ratio of the IC_{50} on Wi-38 versus the four cancer cell lines was estimated. Moreover, cellular morphological changes before and after treatment with the most effective and safest anticancer compounds were investigated using a phase contrast inverted microscope with a digital camera (Olympus, Japan).

4.2.3. Determination of the Redox Alteration in Treated Cancer Cells. The most effective synthetic compounds, NF and 5-FU, were incubated with cancer cell lines (Caco-2, MCF-7, HeLa, and HepG-2) at their safe doses (EC_{100}) in a 5% CO_2 incubator. After 72 h, untreated and treated cancer cells were incubated with 5 μM dihydrodichloro-fluorescein diacetate ($DCFH_2$-DA) in the dark for 30 min at 37 °C. Then, cells were trypsinized and suspended in a fresh phosphate-buffered saline. The percentage of fluorescence DCF product, which generates via the deacetylation and then oxidation of $DCFH_2$ by intercellular reactive oxygen species, was analyzed by a Guava Easycyte flow cytometer (Luminex, Austin, TX, USA) with excitation and emission settings at 488 and 530 nm, respectively.

4.2.4. DNA Binding Studies. 4.2.4.1. Materials. The synthetic dsDNA sequence, 5′- TACCTATCCGTGCCGTGCGAC-3′ and 3′-ATGGATAGGCACGGCACGCTG-5′, was obtained from Integrated DNA Technologies Inc. (Coralville, Iowa) and was purified by standard desalting. The calf thymus DNA (ctDNA) was obtained from Sigma-Aldrich Canada Ltd. (Oakville, Ontario). The EvaGreen (EG) dye was purchased from Biotium Inc. (Fremont, California), sodium chloride was obtained from EMD Chemicals Inc. (Gibbstown, New Jersey), Tris was obtained from ICN Biomedicals (Aurora, Ohio), and ethylenediaminetetraacetic acid (EDTA) was purchased from BDH Inc. (Toronto, Ontario). All chemicals were used as received. A concentration of 10 μM synthetic dsDNA solution was prepared in Tris buffer solution (10 mM Tris, 10 mM NaCl, 1 mM EDTA, pH 7.5), gradually heated to a temperature of 85 °C in a water bath, and then annealed at room temperature (25 °C) in the dark for 24 h before use for all samples.

4.2.4.2. Fluorescence Measurements. Fluorescent biosensors are widely used as sensitive and selective tools for studying DNA interaction with small molecules and detection of any induced DNA damage that may have occurred.[38,57−59] In this study, the EvaGreen (EG) fluorescent biosensor[38] was selected for studying the possible DNA interaction with compound **1**, as a series representative. EG is formed from two fluorescent monomers connected to each other with a flexible linker. As such, EG exists in a closed loop conformation having the two monomers in close proximity (inactive form), thus quenching their fluorescence intensity.[38] While in the presence of the double-stranded DNA (dsDNA), the closed loop conformation opens with the two monomers being far apart in order to bind to the dsDNA. Therefore, maximum fluorescence is observed. In damaged DNA, the normal base pairing is disrupted, affecting EG binding leading to a decrease in the observed fluorescence. The decrease in EG fluorescence is proportional to the induced DNA damage.

For measuring the rate of DNA damage induced by compound **1**, 0.2 μM of the synthetic dsDNA was mixed separately with 0.3 μM EG dye using buffer (10 mM Tris, 10 mM NaCl, 1 mM EDTA, pH 7.5) and incubated at 37 °C for 20 min in the dark and left to cool for 1 h at room temperature, and then 100 μM compound **1** was added separately to the dsDNA-EG mixture. Room temperature fluorescence intensities were recorded at different time intervals for a period of 2.5 h using the Safire fluorescence plate reader with an excitation wavelength of 490 nm and emission wavelength of 530 nm.

For calf thymus DNA (ctDNA) experiments, 0.01 μM ctDNA was mixed with different concentrations of each chemical (0−500 μM). After incubation with 2.0 μM EG dye using buffer (10 mM Tris, 10 mM NaCl, 1 mM EDTA, pH 7.5), fluorescence spectra between 500 and 800 nm with excitation at 490 nm of 100 μL aliquots of such solutions in a 1 cm path length Suprasil quartz fluorescence cuvette were measured.

4.2.5. Cell Cycle Analysis and Apoptotic Investigation for Treated Cancer Cells Using Nuclear Staining Analyses. These assays were conducted as described in our previous work.[2] Briefly, the most effective synthetic compounds, NF and 5-FU, were incubated for 24 or 72 h with cancer cell lines (Caco-2, MCF-7, MDA-MB-231, HeLa, and/or HepG-2) at the indicated concentrations. Afterward, the cell layer was trypsinized, washed with cold PBS and either fixed with 70% ethanol, and stained with the DNA fluorochrome PI after appropriate washing with PBS for the cell cycle assay or treated with annexin V and propidium iodide (PI) for 15 min and then fixed and incubated with 5 μg/mL of streptavidine-fluorescein (Sigma, USA) for 15 min for apoptotic investigation. Samples were analyzed by flowcytometry, while maintaining 10,000 as the number of cells analyzed for each round. Different stages of the cell cycle and apoptosis were estimated by quantification of PI fluorescence and annexin-stained apoptotic cells and PI-stained necrotic cells using flow cytometry, respectively. In addition, cell death in treated cancer cells was investigated using the fluorescence phase contrast microscope (Olympus, Japan) after incubation with double nuclear stains of acridine orange and ethidium bromide (AO-EB).

4.2.6. Immunostaining and Assessment of P-ATM Shuttling. Immunostaining and P-ATM shuttling assessment was performed as described previously.[60] Cells were grown on glass coverslips and treated at 50% confluency with the compounds under investigation at the indicated concentration for 4 h. Afterward, media were removed, and cells were washed with PBS. Cells were then fixed with 4% paraformaldehyde (PFA) in PBS for 20 min and permeabilized with 0.5% Triton X-100 in PBS for 30 min at room temperature. Cells were blocked with blocking buffer (0.1% BSA, 0.2% Triton X-100, 0.05% Tween-20, and 10% normal goat serum in PBS) for 1 h at room temperature. Cells were incubated overnight with 1:200 mouse Anti-ATM antibodies (Santa Cruz Biotechnology, Dallas, TX, USA). Cells were washed with PBS containing 0.1% Tween-20 and incubated with 1:400 Alexa fluor 488-conjugated goat anti-mouse Ig for 1 h at room temperature. After washing, cells were mounted on microscope slides, using Fluoroshield mounting medium with DAPI (4′,6′-diamidino-2-

https://doi.org/10.1021/acs.jmedchem.2c01408
J. Med. Chem. 2023, 66, 4565−4587

phenyl-indole) (Abcam, Cambridge, UK), and examined with a Zeiss LSM 710 confocal fluorescent microscope (Zeiss Germany). Fluorescent nuclear P-ATM foci were counted per nucleus by two blinded reviewers.

4.2.7. Western Blotting. Western blotting was performed on cellular extracts following 24 h incubation with compound **1** at the indicated concentration as described in our previous work.[2] MCF-7 cells (2×10^6) were seeded in T75 flasks and allowed to reach 70% confluency before treatment with either DMSO or compound **1** at the indicated concentration for 24 h. The medium was aspirated and cells were washed with 1× phosphate-buffered saline (PBS, Sigma-Aldrich) and scrapped, and proteins were extracted and subjected to SDS-PAGE as described previously.[61] A 1:1000 concentration of polyclonal rabbit anti-p53 (Cell Signaling, Danvers, MA) was used. Band intensity was normalized to GAPDH as a loading control. A clarity max ECL western blotting kit from Bio-rad was used to visualize the bands, and a Bio-rad ChemiDoc unit (Bio-rad, Hercules, CA, USA) was used to capture the chemiluminescence signal.

4.2.8. MDM2−p53 Complex Sandwich ELISA. MDM2−p53 complex sandwich ELISA (Becton-Dickinson, Franklin Lakes, NJ, USA) was performed according to manufacturer's instructions as previously reported.[62] A cocktail mixture of recombinant human p53 protein (Abcam, Cambridge, UK) and recombinant human MDM2 (Abcam, Cambridge, UK) was prepared and then subjected to treatment with serial concentrations (1, 0.2, 0.04, and 0.008 μM) of the test compounds for 10 min. Afterward, 10 μL of the samples was transferred to the test plate and the signals were recorded. Absorbance was measured at 450 nm with an ELISA reader (Robonik, Ambernath, India). Measurements were plotted versus the established p53 standard curve for the ic50 estimation.

4.2.9. Clonogenic Assay. UC3 cells were seeded at a density of 50,000 cells per well in 12-well plates and were allowed to adhere overnight. Cells were irradiated with a 225 kV Precision X-Ray irradiator (Techna, Toronto, Canada). Irradiation was performed at 3 Gy/min, and a 1.5 mm Aluminum filter was used. Following compound **1** treatments for 24 h, cells were washed with PBS, trypsinized, and counted. 4000 cells from each condition were then seeded in 6-well plates for 7 days. Cells were then washed with PBS, fixed with 95% ethanol, and stained with 0.2% crystal violet for 5 min. Viable cellular colonies with more than 50 cells were counted and were expressed relative to those of the vehicle treated condition.

4.2.10. Real-Time Quantitative PCR Analysis for Bcl-2 and Bax. Cancer cell lines (Caco-2, MCF-7, HeLa, and HepG-2) were incubated with the safe doses (EC_{100}) of the most effective synthetic compounds as well as NF and 5-FU for 72 h in a 5% CO_2 incubator. RNAs of untreated and treated cancer cells were extracted using a Gene JET RNA purification kit (Thermo Scientific, USA). Then, cDNAs were synthesized using a cDNA Synthesis Kit (Thermo Scientific, USA). Real-time PCR was performed using a SYBR green master mix, and specific primers (forward/reverse) were 5′-TCCGATCAGGAAGGC-TAGAGTT-3′/5′-TCGGTCTCCTAA-AAGCAGGC-3′ for Bcl-2 and 5′-CCGCCGTGGACACAGAC-3′/5′-CAGAAAACATGT-CAGCTGCCA-3′ for Bax. The thermal cycling parameters were pre-denaturation followed by 40 amplification cycles of 1 min at 95 °C and 30 s at 60 °C and at 72 °C for 30 s. GAPDH mRNA was quantified to adjust the amount of mRNA in each sample. The $2^{-\Delta\Delta CT}$ equation was used to estimate the change in gene expressions before and after treatment of cancer cells, and then the expression fold ratio between Bax and Bcl-2 was calculated.

4.2.11. Caspase-Glo 3/7 Apoptosis Assay. After exposure cancer cell lines (Caco-2, MCF-7, HeLa, and HepG-2) for 72 h to the safe doses (EC_{100}) of **1**, **2e**, **4b**, NF, and **5-FU** in a 5% CO_2 incubator, caspases 3 and 7 activation was quantified according to the instructions from the manufacturer (Promega, USA). Briefly, 100 μL of Caspase-Glo 3/7 substrate was added to untreated and treated cancer cell lines and incubated for 2 h in a 5% CO_2 incubator. Subsequently, plates were analyzed using a fluorescence omega microplate reader (BMG LabTech, Germany) at 490 nm excitation and 520 nm emission. The increase in luminescence signals is equivalent to an elevation in the caspase activity.

4.2.12. Determination of the Correlation between the Prooxidant Effect and Apoptotic Potential of the most Effective Safe Compounds. Serial concentrations (within safe dose range) of **4b** and **1** were incubated with HeLa and HepG-2 cells, respectively, while serial concentrations (within safe dose range) of **2e** were incubated with Caco-2 and MCF-7 for 72 h in a 5% CO_2 incubator. Then, untreated and treated cancer cells were stained with DCF and annexin/PI, separately, for detection percentage of DCF oxidation and apoptosis using flow cytometry as demonstrated above. Also, ratio of Bax/Bcl-2 was detected using real-time PCR as described above. Correlation between % DCF oxidation and both % apoptosis and Bax/Bcl-2 ratio was determined by estimation of the Pearson correlation coefficient (r) using Graphpad prism software. A positive value of r indicates positive correlation and when r equals 1 or is above 0.9, it is a sign for strong correlation.

*4.2.13. In Vivo Validation of the Antitumor Effect of Compound **1**.* All animal experiments were conducted according to a protocol that was approved by our Institutional Animal Care and Use Committee (ALEXU-IACUC, Approval no. AU-06-2022-10-15-3-131 dated 15/10/2022) and in accordance with the NIH Guide for Care and Use of Laboratory Animals, eighth edition.[63] A MCF-7 tumor xenograft in the immunocompromised BALB/c mouse model was used for the assessment of the *in vivo* antitumor activity and relative safety of compound **1** as described in our previous work.[28] Briefly, adult BALB/c mice housed in a pathogen-free environment with *ad libitum* access to food and a 12 h dark/light cycle were rendered immunosuppressed by a daily intraperitoneal injection of cyclosporin (CsA, Neoral injection, Novartis Pharmaceuticals) at 80 mg/kg for 4 days before MCF-7 cell injection. A suspension of two million MCF-7 cells in 200 μL of DMEM was injected subcutaneously in the interscapular region in mice. After a palpable tumor mass with a volume of around 1 cm^3 developed, the tumor-bearing mice were randomly divided into four groups of five mice; the control (vehicle-treated) group, 5-FU-treated group, NF-treated group, and compound **1**-treated group. The drugs were administered daily by subcutaneous injection at their respective doses for 21 days. The overall conditions of mice, including food intake and body weight, were followed up daily, and mortality was recorded. Three days after the conclusion of drug treatment, all mice were euthanized by cervical dislocation after isoflurane anesthesia. A skin incision was used to expose the subcutaneous layer of the interscapular region in mice. Tumors were photographed and then excised and weighed on a sensitive balance.

4.2.14. Statistical Analysis. Data were expressed as mean ± standard error of the mean (SEM). Statistical significance was estimated by the appropriate statistical test as indicated in the corresponding figure legends using GraphPad Prism. The differences were considered statistically significant at $p < 0.05$.

4.3. Molecular Docking. The docking studies were conducted using MOE 2019.0102 software (Chemical Computing Group, Montreal, Canada) using the crystal structure of human MDM2 protein active site (PDB 3LBL), as previously described.[64] Hydrogen atoms were added to the database of test compounds, partial charges were computed, and energy minimization was supported by Force Field MMFF94x. Unnecessary protein chains, water molecules, and surfactant molecules were also discarded. We used MOE's default settings, which comprised a triangle matcher as a placement technique and London dG as the main scoring function, with GBVI/WSA dG scoring as an extra refinement step. We selected the ideal poses in terms of both energy score and binding interactions. This was performed using the scoring algorithms and visual assessment of the hydrogen bonding, hydrophobic, and ionic contacts with the binding pocket residues.

■ ASSOCIATED CONTENT

Supporting Information

The Supporting Information is available free of charge at https://pubs.acs.org/doi/10.1021/acs.jmedchem.2c01408.

^{1}H NMR and ^{13}C NMR spectra; and HPLC purity analyses (PDF)

https://doi.org/10.1021/acs.jmedchem.2c01408
J. Med. Chem. 2023, 66, 4565−4587

SMILES chemical notation for the final compounds (CSV)
PDB files of ligand bound docking (PDB)

AUTHOR INFORMATION

Corresponding Authors

Ahmed F. El-Yazbi − *Faculty of Pharmacy and the Research and Innovation Hub, Alamein International University, Alamein 5060335, Egypt; Department of Pharmacology and Toxicology, American University of Beirut, Beirut 11072020, Lebanon; Department of Pharmacology and Toxicology, Faculty of Pharmacy, Alexandria University, Alexandria 21521, Egypt*; Email: ahmed.fawzy.aly@alexu.edu.eg

Ahmed S. F. Belal − *Department of Pharmaceutical Chemistry, Faculty of Pharmacy, Alexandria University, Alexandria 21521, Egypt*; orcid.org/0000-0001-9463-0844; Email: ahmed.belal@alexu.edu.eg

Authors

Perihan A. Elzahhar − *Department of Pharmaceutical Chemistry, Faculty of Pharmacy, Alexandria University, Alexandria 21521, Egypt*; orcid.org/0000-0003-2665-6019

Hisham A. Nematalla − *Department of Pharmacology and Toxicology, Faculty of Pharmacy, Damanhour University, Damanhour 22516, Egypt*

Houssam Al-Koussa − *Department of Pharmacology and Toxicology, American University of Beirut, Beirut 11072020, Lebanon*

Carla Abrahamian − *Walther Straub Institute of Pharmacology and Toxicology, Faculty of Medicine, Ludwig-Maximilians-University, 80336 Munich, Germany*

Amira F. El-Yazbi − *Department of Pharmaceutical Analytical Chemistry, Faculty of Pharmacy, Alexandria University, Alexandria 21521, Egypt*; orcid.org/0000-0002-1717-5291

Larry Bodgi − *Department of Radiation Oncology, American University of Beirut Medical Center, Beirut 11072020, Lebanon; Department of Anatomy, Cell Biology and Physiological Sciences, Faculty of Medicine, American University of Beirut, Beirut 11072020, Lebanon*

Jolie Bou-Gharios − *Department of Radiation Oncology, American University of Beirut Medical Center, Beirut 11072020, Lebanon; Department of Anatomy, Cell Biology and Physiological Sciences, Faculty of Medicine, American University of Beirut, Beirut 11072020, Lebanon*

Joyce Azzi − *Department of Radiation Oncology, American University of Beirut Medical Center, Beirut 11072020, Lebanon; Department of Anatomy, Cell Biology and Physiological Sciences, Faculty of Medicine, American University of Beirut, Beirut 11072020, Lebanon*

Joelle Al Choboq − *Department of Radiation Oncology, American University of Beirut Medical Center, Beirut 11072020, Lebanon; Department of Anatomy, Cell Biology and Physiological Sciences, Faculty of Medicine, American University of Beirut, Beirut 11072020, Lebanon*

Hala F. Labib − *Department of Pharmaceutical Chemistry, College of Pharmacy, Arab Academy of Science Technology and Maritime Transport, Alexandria 21913, Egypt*

Wassim Abou Kheir − *Department of Anatomy, Cell Biology and Physiological Sciences, Faculty of Medicine, American University of Beirut, Beirut 11072020, Lebanon*; orcid.org/0000-0001-9719-9324

Marwa M. Abu-Serie − *Medical Biotechnology Department, Genetic Engineering and Biotechnology Research Institute, City of Scientific Research and Technological Applications (SRTA-City), Alexandria 21934, Egypt*

Mohamed A. Elrewiny − *Faculty of Pharmacy and the Research and Innovation Hub, Alamein International University, Alamein 5060335, Egypt*

Complete contact information is available at: https://pubs.acs.org/10.1021/acs.jmedchem.2c01408

Author Contributions

$^{\nabla}$P.A.E. and H.A.N. contributed equally to this work.

Notes

The authors declare no competing financial interest.

ABBREVIATIONS USED

AO, acridine orange; ATM, ataxia telangiectasia mutated protein; BIODS, biology-oriented drug synthesis; CHK2, checkpoint kinase 2; DCFH-DA, dihydrodichlorofluorescein diacetate; DOX, doxorubicin; DSB, double-strand breaks; EB, ethidium bromide; EG, EvaGreen; LOD, limit of detection; LOQ, limit of quantification; MDM2, mouse double minute 2; NF, nitrofurantoin; ROS, reactive oxygen species; SI, selectivity index; STAT3, signal transducer and activator of transcription 3

REFERENCES

(1) Perlmutter, J. I.; Forbes, L. T.; Krysan, D. J.; Ebsworth-Mojica, K.; Colquhoun, J. M.; Wang, J. L.; Dunman, P. M.; Flaherty, D. P. Repurposing the Antihistamine Terfenadine for Antimicrobial Activity against Staphylococcus Aureus. *J. Med. Chem.* **2014**, *57*, 8540−8562.

(2) Chaaban, I.; Hafez, H.; AlZaim, I.; Tannous, C.; Ragab, H.; Hazzaa, A.; Ketat, S.; Ghoneim, A.; Katary, M.; Abd-Alhaseeb, M. M.; Zouein, F. A.; Albohy, A.; Amer, A. N.; El-Yazbi, A. F.; Belal, A. S. F. Transforming Iodoquinol into Broad Spectrum Anti-Tumor Leads: Repurposing to Modulate Redox Homeostasis. *Bioorg. Chem.* **2021**, *113*, 105035.

(3) Zuma, N. H.; Aucamp, J.; N'Da, D. D. An Update on Derivatisation and Repurposing of Clinical Nitrofuran Drugs. *Eur. J. Pharm. Sci.* **2019**, *140*, 105092.

(4) Sleire, L.; Førde, H. E.; Netland, I. A.; Leiss, L.; Skeie, B. S.; Enger, P. Ø. Drug Repurposing in Cancer. *Pharmacol. Res.* **2017**, *124*, 74−91.

(5) Sonaye, H. V.; Sheikh, R. Y.; Doifode, C. A. Drug Repurposing: Iron in the Fire for Older Drugs. *Biomed. Pharmacother.* **2021**, *141*, 111638.

(6) Parvathaneni, V.; Kulkarni, N. S.; Muth, A.; Gupta, V. Drug Repurposing: A Promising Tool to Accelerate the Drug Discovery Process. *Drug Discovery Today* **2019**, *24*, 2076−2085.

(7) Nowak-Sliwinska, P.; Scapozza, L.; Altaba, A. R. i. Drug Repurposing in Oncology: Compounds, Pathways, Phenotypes and Computational Approaches for Colorectal Cancer. *Biochim. Biophys. Acta - Rev. Cancer* **2019**, *1871*, 434−454.

(8) Yeh, C.; Cheng, C.-C.; Lin, H.-C.; Luo, T.-Y.; Chang, J.; Ho, A.-S. Pravastatin Inhibits Tumor Growth through Elevating the Levels of Apolipoprotein A1. *Adv. Dig. Med.* **2016**, *3*, 3−10.

(9) Van Nuffel, A. M. T. Repurposing Drugs in Oncology (ReDO)—Clarithromycin as an Anti-Cancer Agent. *Ecancermedicalscience* **2015**, *9*, 1−26.

(10) Taha, M.; Imran, S.; Ismail, N. H.; Selvaraj, M.; Rahim, F.; Chigurupati, S.; Ullah, H.; Khan, F.; Salar, U.; Javid, M. T.; Vijayabalan, S.; Zaman, K.; Khan, K. M. Biology-Oriented Drug Synthesis (BIODS) of 2-(2-Methyl-5-Nitro-1H-Imidazol-1-Yl)Ethyl Aryl Ether Derivatives, in Vitro α-Amylase Inhibitory Activity and in Silico Studies. *Bioorg. Chem.* **2017**, *74*, 1−9.

(11) Salar, U.; Khan, K. M.; Taha, M.; Ismail, N. H.; Ali, B.; Qurat-ul-Ain; Perveen, S.; Ghufran, M.; Wadood, A. Biology-Oriented Drug Synthesis (BIODS): In Vitro β-Glucuronidase Inhibitory and in Silico

Studies on 2-(2-Methyl-5-Nitro-1H-Imidazol-1-Yl)Ethyl Aryl Carboxylate Derivatives. *Eur. J. Med. Chem.* **2017**, *125*, 1289−1299.
(12) Khan, M.; Alam, A.; Khan, K. M.; Salar, U.; Chigurupati, S.; Wadood, A.; Ali, F.; Mohammad, J. I.; Riaz, M.; Perveen, S. Flurbiprofen Derivatives as Novel α-Amylase Inhibitors: Biology-Oriented Drug Synthesis (BIODS), in Vitro, and in Silico Evaluation. *Bioorg. Chem.* **2018**, *81*, 157−167.
(13) https://gco.iarc.fr/today/data/factsheets/cancers/39-All-cancers-fact-sheet.pdf.
(14) Andrade, J. K. F.; Souza, M. I. F.; Gomes Filho, M. A.; Silva, D. M. F.; Barros, A. L. S.; Rodrigues, M. D.; Silva, P. B. N.; Nascimento, S. C.; Aguiar, J. S.; Brondani, D. J.; Militão, G. C. G.; Silva, T. G. N-Pentyl-Nitrofurantoin Induces Apoptosis in HL-60 Leukemia Cell Line by Upregulating BAX and Downregulating BCL-XL Gene Expression. *Pharmacol. Rep.* **2016**, *68*, 1046−1053.
(15) Beloglazkina, A.; Zyk, N.; Majouga, A.; Beloglazkina, E. Recent Small-Molecule Inhibitors of the P53−MDM2 Protein−Protein Interaction. *Molecules* **2020**, *25*, 1211.
(16) Carr, M. I.; Jones, S. N. Regulation of the Mdm2-P53 Signaling Axis in the DNA Damage Response and Tumorigenesis. *Transl. Cancer Res.* **2016**, *5*, 707−724.
(17) Lane, D. P. P53, Guardian of the Genome. *Nature* **1992**, *358*, 15−16.
(18) Raycroft, L.; Wu, H.; Lozano, G. Transcriptional Activation by Wild-Type but Not Transforming Mutants of the P53 Anti-Oncogene. *Science* **1990**, *249*, 1049−1051.
(19) Pant, V.; Xiong, S.; Jackson, J. G.; Post, S. M.; Abbas, H. A.; Quintás-Cardama, A.; Hamir, A. N.; Lozano, G. The P53−Mdm2 Feedback Loop Protects against DNA Damage by Inhibiting P53 Activity but Is Dispensable for P53 Stability, Development, and Longevity. *Genes Dev.* **2013**, *27*, 1857−1867.
(20) Weber, A. M.; Ryan, A. J. ATM and ATR as Therapeutic Targets in Cancer. *Pharmacol. Ther.* **2015**, *149*, 124−138.
(21) Canman, C. E.; Lim, D.-S.; Cimprich, K. A.; Taya, Y.; Tamai, K.; Sakaguchi, K.; Appella, E.; Kastan, M. B.; Siliciano, J. D. Activation of the ATM Kinase by Ionizing Radiation and Phosphorylation of P53. *Science* **1998**, *281*, 1677−1679.
(22) Marine, J.-C.; Lozano, G. Mdm2-Mediated Ubiquitylation: P53 and Beyond. *Cell Death Differ.* **2010**, *17*, 93−102.
(23) Sullivan, K. D.; Gallant-Behm, C. L.; Henry, R. E.; Fraikin, J. L.; Espinosa, J. M. The P53 Circuit Board. *Biochim. Biophys. Acta - Rev. Cancer* **2012**, *1825*, 229−244.
(24) Bailly, C. Toward a Repositioning of the Antibacterial Drug Nifuroxazide for Cancer Treatment. *Drug Discovery Today* **2019**, *24*, 1930−1936.
(25) Zhu, Y.; Ye, T.; Yu, X.; Lei, Q.; Yang, F.; Xia, Y.; Song, X.; Liu, L.; Deng, H.; Gao, T.; Peng, C.; Zuo, W.; Xiong, Y.; Zhang, L.; Wang, N.; Zhao, L.; Xie, Y.; Yu, L.; Wei, Y. Nifuroxazide Exerts Potent Anti-Tumor and Anti-Metastasis Activity in Melanoma. *Sci. Rep.* **2016**, *6*, 20253.
(26) Graves, B.; Thompson, T.; Xia, M.; Janson, C.; Lukacs, C.; Deo, D.; Di Lello, P.; Fry, D.; Garvie, C.; Huang, K.-S.; Gao, L.; Tovar, C.; Lovey, A.; Wanner, J.; Vassilev, L. T. Activation of the P53 Pathway by Small-Molecule-Induced MDM2 and MDMX Dimerization. *Proc. Natl. Acad. Sci.* **2012**, *109*, 11788−11793.
(27) Upadhyay, N.; Tilekar, K.; Loiodice, F.; Anisimova, N. Y.; Spirina, T. S.; Sokolova, D. V.; Smirnova, G. B.; Choe, J.; Meyer-Almes, F.-J.; Pokrovsky, V. S.; Lavecchia, A.; Ramaa, C. Pharmacophore Hybridization Approach to Discover Novel Pyrazoline-Based Hydantoin Analogs with Anti-Tumor Efficacy. *Bioorg. Chem.* **2021**, *107*, 104527.
(28) Elzahhar, P. A.; Abd El Wahab, S. M.; Elagawany, M.; Daabees, H.; Belal, A. S. F.; EL-Yazbi, A. F.; Eid, A. H.; Alaaeddine, R.; Hegazy, R. R.; Allam, R. M.; Helmy, M. W.; Elgendy, B.; Angeli, A.; El-Hawash, S. A.; Supuran, C. T. Expanding the Anticancer Potential of 1,2,3-Triazoles via Simultaneously Targeting Cyclooxygenase-2, 15-Lipoxygenase and Tumor-Associated Carbonic Anhydrases. *Eur. J. Med. Chem.* **2020**, *200*, 112439.
(29) Temraz, M. G.; Elzahhar, P. A.; El-Din A. Bekhit, A.; Bekhit, A. A.; Labib, H. F.; Belal, A. S. F. Anti-Leishmanial Click Modifiable Thiosemicarbazones: Design, Synthesis, Biological Evaluation and in Silico Studies. *Eur. J. Med. Chem.* **2018**, 151.
(30) Elzahhar, P. A.; Alaaeddine, R.; Ibrahim, T. M.; Nassra, R.; Ismail, A.; Chua, B. S. K.; Frkic, R. L.; Bruning, J. B.; Wallner, N.; Knape, T.; von Knethen, A.; Labib, H.; El-Yazbi, A. F.; Belal, A. S. F. Shooting Three Inflammatory Targets with a Single Bullet: Novel Multi-Targeting Anti-Inflammatory Glitazones. *Eur. J. Med. Chem.* **2019**, *167*, 562−582.
(31) Abu-Serie, M. M.; El-Rashidy, H. F. In Vitro Collapsing Colon Cancer Cells by Selectivity of Disulfiram-Loaded Charge Switchable Nanoparticles Against Cancer Stem Cells. *Recent Pat. Anti-Cancer Drug Discovery* **2017**, 260−271.
(32) Prayong, P.; Barusrux, S.; Weerapreeyakul, N. Cytotoxic Activity Screening of Some Indigenous Thai Plants. *Fitoterapia* **2008**, *79*, 598−601.
(33) Mani, S.; Balasubramanian, M. G.; Ponnusamy, P.; Vijayan, P. Antineoplastic Effect of PAC Capped Silver Nanoparticles Promote Apoptosis in HT-29 Human Colon Cancer Cells. *J. Cluster Sci.* **2019**, *30*, 483−493.
(34) del García-Rodríguez, M. C.; Carvente-Juárez, M. M.; Altamirano-Lozano, M. A. Antigenotoxic and Apoptotic Activity of Green Tea Polyphenol Extracts on Hexavalent Chromium-Induced DNA Damage in Peripheral Blood of CD-1 Mice: Analysis with Differential Acridine Orange/Ethidium Bromide Staining. *Oxid. Med. Cell. Longevity* **2013**, *2013*, 1−9.
(35) Riyasdeen, A.; Senthilkumar, R.; Periasamy, V. S.; Preethy, P.; Srinag, S.; Zeeshan, M.; Krishnamurthy, H.; Arunachalam, S.; Akbarsha, M. A. Antiproliferative and Apoptosis-Induction Studies of a Metallosurfactant in Human Breast Cancer Cell MCF-7. *RSC Adv.* **2014**, *4*, 49953−49959.
(36) Tsuchiya, T.; Kijima, A.; Ishii, Y.; Takasu, S.; Yokoo, Y.; Nishikawa, A.; Yanai, T.; Umemura, T. Role of Oxidative Stress in the Chemical Structure-Related Genotoxicity of Nitrofurantoin in Nrf2-Deficient Gpt Delta Mice. *J. Toxicol. Pathol.* **2018**, *31*, 169−178.
(37) Poudel, B. K.; Choi, J.; Park, J. H.; Doh, K.-O.; Byeon, J. H. In Vitro Exposure of Simulated Meat-Cooking Fumes to Assess Adverse Biological Effects. *Sci. Rep.* **2017**, *7*, 10841.
(38) El-Yazbi, A. F.; Loppnow, G. R. Probing DNA Damage Induced by Common Antiviral Agents Using Multiple Analytical Techniques. *J. Pharm. Biomed. Anal.* **2018**, *157*, 226−234.
(39) Thorn, C. F.; Oshiro, C.; Marsh, S.; Hernandez-Boussard, T.; McLeod, H.; Klein, T. E.; Altman, R. B. Doxorubicin Pathways: Pharmacodynamics and Adverse Effects. *Pharmacogenet. Genomics* **2011**, *21*, 440−446.
(40) Hui, L.; Zheng, Y.; Yan, Y.; Bargonetti, J.; Foster, D. A. Mutant P53 in MDA-MB-231 Breast Cancer Cells Is Stabilized by Elevated Phospholipase D Activity and Contributes to Survival Signals Generated by Phospholipase D. *Oncogene* **2006**, *25*, 7305−7310.
(41) Marchenko, N. D.; Moll, U. M. Mitochondrial Death Functions of P53. *Mol. Cell. Oncol.* **2014**, *1*, No. e955995.
(42) Basu, A.; Haldar, S. The Relationship between BcI2, Bax and P53: Consequences for Cell Cycle Progression and Cell Death. *Mol. Hum. Reprod.* **1998**, *4*, 1099−1109.
(43) Paul-Samojedny, M.; Kokocińska, D.; Samojedny, A.; Mazurek, U.; Partyka, R.; Lorenz, Z.; Wilczok, T. Expression of Cell Survival/Death Genes: Bcl-2 and Bax at the Rate of Colon Cancer Prognosis. *Biochim. Biophys. Acta - Mol. Basis Dis.* **2005**, *1741*, 25−29.
(44) Raisova, M.; Hossini, A. M.; Eberle, J.; Riebeling, C.; Orfanos, C. E.; Geilen, C. C.; Wieder, T.; Sturm, I.; Daniel, P. T. The Bax/Bcl-2 Ratio Determines the Susceptibility of Human Melanoma Cells to CD95/Fas-Mediated Apoptosis. *J. Invest. Dermatol.* **2001**, *117*, 333−340.
(45) Sakamaki, K.; Satou, Y. Caspases: Evolutionary Aspects of Their Functions in Vertebrates. *J. Fish Biol.* **2009**, *74*, 727−753.
(46) Lakhani, S. A.; Masud, A.; Kuida, K.; Porter, G. A.; Booth, C. J.; Mehal, W. Z.; Inayat, I.; Flavell, R. A. Caspases 3 and 7: Key Mediators of Mitochondrial Events of Apoptosis. *Science* **2006**, *311*, 847−851.

https://doi.org/10.1021/acs.jmedchem.2c01408
J. Med. Chem. 2023, 66, 4565−4587

(47) Cao, Z.; Zhang, Z.; Huang, Z.; Wang, R.; Yang, A.; Liao, L.; DU, J. Antitumor and Immunomodulatory Effects of Low-Dose 5-FU on Hepatoma 22 Tumor-Bearing Mice. *Oncol. Lett.* **2014**, *7*, 1260−1264.
(48) Zhang, S.; Liu, Y.; Xiang, D.; Yang, J.; Liu, D.; Ren, X.; Zhang, C. Assessment of Dose-Response Relationship of 5-Fluorouracil to Murine Intestinal Injury. *Biomed. Pharmacother.* **2018**, *106*, 910−916.
(49) Fučić, A.; Marković, D.; Ferenčić, Z.; Mildner, B.; Jazbec, A. M.; Špoljar, J. B. Comparison of Genomic Damage Caused by 5-Nitrofurantoin in Young and Adult Mice Using the in Vivo Micronucleus Assay. *Environ. Mol. Mutagen.* **2005**, *46*, 59−63.
(50) Yeo, S. J.; Jin, C. M.; Kim, S. Y.; Park, H. In Vitro and in Vivo Effects of Nitrofurantoin on Experimental Toxoplasmosis. *Korean J. Parasitol.* **2016**, *54*, 155−161.
(51) Yasmin, S.; Capone, F.; Laghezza, A.; Piaz, F. D.; Loiodice, F.; Vijayan, V.; Devadasan, V.; Mondal, S. K.; Atll, Ö.; Baysal, M.; Pattnaik, A. K.; Jayaprakash, V.; Lavecchia, A. Novel Benzylidene Thiazolidinedione Derivatives as Partial PPARγ Agonists and Their Antidiabetic Effects on Type 2 Diabetes. *Sci. Rep.* **2017**, *7*, 1−17.
(52) Khoury, K.; Popowicz, G. M.; Holak, T. A.; Dömling, A. The P53-MDM2/MDMX Axis − A Chemotype Perspective. *Medchemcomm* **2011**, *2*, 246.
(53) Fu, T.; Min, H.; Xu, Y.; Chen, J.; Li, G. Molecular Dynamic Simulation Insights into the Normal State and Restoration of P53 Function. *Int. J. Mol. Sci.* **2012**, 9709−9740.
(54) Popowicz, G. M.; Czarna, A.; Wolf, S.; Wang, K.; Wang, W.; Dömling, A.; Holak, T. A. Structures of Low Molecular Weight Inhibitors Bound to MDMX and MDM2 Reveal New Approaches for P53-MDMX/MDM2 Antagonist Drug Discovery. *Cell Cycle* **2010**, *9*, 1104−1111.
(55) Zuma, N. H.; Smit, F. J.; Seldon, R.; Aucamp, J.; Jordaan, A.; Warner, D. F.; N'Da, D. D. Single-Step Synthesis and in Vitro Anti-Mycobacterial Activity of Novel Nitrofurantoin Analogues. *Bioorg. Chem.* **2020**, *96*, 103587.
(56) Mosmann, T. Rapid Colorimetric Assay for Cellular Growth and Survival: Application to Proliferation and Cytotoxicity Assays. *J. Immunol. Methods* **1983**, *65*, 55−63.
(57) El-Yazbi, A. F.; Loppnow, G. R. Detecting UV-Induced Nucleic-Acid Damage. *TrAC Trends Anal. Chem.* **2014**, *61*, 83−91.
(58) El-Yazbi, A. F.; Guirguis, K. M.; Belal, T. S.; Bedair, M. M. Sensitive Spectrofluorimetric and Mass Spectroscopic Methods for the Determination of Nucleic Acid Damage Induced by Photosensitized Anti-Inflammatory Drugs: Comparative Study. *J. Pharm. Biomed. Anal.* **2020**, *187*, 113326.
(59) El-Yazbi, A.; Loppnow, G. R. Locked Nucleic Acid Hairpin Detection of UV-Induced DNA Damage. *Can. J. Chem.* **2011**, *89*, 402−408.
(60) Al Bitar, S.; Ballout, F.; Monzer, A.; Kanso, M.; Saheb, N.; Mukherji, D.; Faraj, W.; Tawil, A.; Doughan, S.; Hussein, M.; Abou-Kheir, W.; Gali-Muhtasib, H. Thymoquinone Radiosensitizes Human Colorectal Cancer Cells in 2D and 3D Culture Models. *Cancers* **2022**, DOI: 10.3390/cancers14061363.
(61) AlFadly, E. D.; Elzahhar, P. A.; Tramarin, A.; Elkazaz, S.; Shaltout, H.; Abu-Serie, M. M.; Janockova, J.; Soukup, O.; Ghareeb, D. A.; El-Yazbi, A. F.; Rafeh, R. W.; Bakkar, N.-M. Z.; Kobeissy, F.; Iriepa, I.; Moraleda, I.; Saudi, M. N. S.; Bartolini, M.; Belal, A. S. F. Tackling Neuroinflammation and Cholinergic Deficit in Alzheimer's Disease: Multi-Target Inhibitors of Cholinesterases, Cyclooxygenase-2 and 15-Lipoxygenase. *Eur. J. Med. Chem.* **2019**, *167*, 161−186.
(62) Ibrahim, H. S.; Eldehna, W. M.; Fallacara, A. L.; Ahmed, E. R.; Ghabbour, H. A.; Elaasser, M. M.; Botta, M.; Abou-seri, S. M.; Abdel-Aziz, H. A. One-Pot Synthesis of Spiro(Indoline-3,4′-Pyrazolo[3,4-b]Pyridine)-5′-Carbonitriles as P53-MDM2 Interaction Inhibitors. *Future Med. Chem.* **2018**, *10*, 2771−2789.
(63) National Research Council. Guide for the Care and Use of Laboratory Animals. *Guid. Care Use Lab. Anim.* **2011**, 10.17226/12910.
(64) Elzahhar, P. A.; Alaaeddine, R. A.; Nassra, R.; Ismail, A.; Labib, H. F.; Temraz, M. G.; Belal, A. S. F.; El-Yazbi, A. F. Challenging Inflammatory Process at Molecular, Cellular and in Vivo Levels via Some New Pyrazolyl Thiazolones. *J. Enzyme Inhib. Med. Chem.* **2021**, *36*, 669−684.

https://doi.org/10.1021/acs.jmedchem.2c01408
J. Med. Chem. 2023, 66, 4565−4587